Medical Physics
The International Journal of Medical Physics Research and Practice

Oblique reconstructions in tomosynthesis. I. Linear systems theory

Raymond J. Acciavatti and Andrew D. A. Maidment

Citation: Medical Physics **40**, 111911 (2013); doi: 10.1118/1.4819941
View online: http://dx.doi.org/10.1118/1.4819941
View Table of Contents: http://scitation.aip.org/content/aapm/journal/medphys/40/11?ver=pdfcov
Published by the American Association of Physicists in Medicine

Oblique reconstructions in tomosynthesis. I. Linear systems theory

Raymond J. Acciavatti and Andrew D. A. Maidment[a)]
Department of Radiology, Perelman School of Medicine at the University of Pennsylvania, Philadelphia, Pennsylvania 19104-4206

(Received 18 May 2013; revised 4 August 2013; accepted for publication 12 August 2013; published 11 October 2013)

Purpose: By convention, slices in a tomosynthesis reconstruction are created on planes parallel to the detector. It has not yet been demonstrated that slices can be generated along oblique directions through the same volume, analogous to multiplanar reconstructions in computed tomography (CT). The purpose of this work is to give a proof-of-principle justification for oblique reconstructions in tomosynthesis, which acquires projection images over a smaller angular range than CT.
Methods: To investigate the visibility of individual frequencies in an oblique reconstruction, a theoretical framework is developed in which the reconstruction of a sinusoidal input is calculated. The test frequency is pitched at an angle in a 2D parallel-beam acquisition geometry. Reconstructions are evaluated along the pitch of the object. The modulation transfer function (MTF) is calculated from the relative signal at various test frequencies. The MTF determines whether modulation is within detectable limits in oblique reconstructions. In the previous linear systems (LS) model [B. Zhao and W. Zhao, "Three-dimensional linear system analysis for breast tomosynthesis," Med. Phys. **35**(12), 5219–5232 (2008)], the MTF was calculated only in reconstructed slices parallel to the detector. This paper generalizes the MTF calculation to reconstructed slices at all possible pitches. Unlike the previous LS model, this paper also analyzes the effect of object thickness on the MTF. A second test object that is considered is a rod whose long axis is pitched similar to the sinusoidal input. The rod is used to assess whether the length of an object can be correctly estimated in oblique reconstructions.
Results: To simulate the conventional display of the reconstruction, slices are first created along a 0° pitch. This direction is perpendicular to the rays of the central projection. The authors show that the input frequency of a pitched sinusoidal object cannot be determined using these slices. By changing the pitch of the slice to match the object, it is shown that the input frequency is properly resolved. To prove that modulation is preserved in pitched slices, the MTF is also calculated. Modulation is within detectable limits over a broad range of pitches if the object is thin, but is detectable over a narrower range of pitches if the object is thick. Turning next to the second test object, it is shown that the length of a pitched rod can be correctly determined in oblique reconstructions. Concordant with the behavior of the MTF, the length estimate is accurate over a broad range of pitches if the object is thin, but is correct over a narrower range of pitches if the object is thick.
Conclusions: This work justifies the feasibility of oblique reconstructions in tomosynthesis. It is demonstrated that pitched test objects are most easily visualized with oblique reconstructions instead of conventional reconstructions. In order to achieve high image quality over a broad range of pitches, the object must be thin. By analyzing the effect of reconstruction pitch and object thickness on image quality, this paper generalizes the previous LS model for tomosynthesis. [http://dx.doi.org/10.1118/1.4819941]

Key words: tomosynthesis, multiplanar reconstruction (MPR), oblique reconstruction, filtered backprojection (FBP), modulation transfer function (MTF)

1. INTRODUCTION

In computed tomography (CT), axial slices of the body are reconstructed successively as the patient is translated in the longitudinal direction. Due to the near isotropic resolution of modern CT scanners, the stack of axial slices can be reformatted to display a multiplanar reconstruction (MPR), or an image of any planar or curved surface in the volume. One application of MPR is visualizing stenosis in coronary arteries with a curved surface following the contour of the vessel. Another example is dental CT, in which an oblique plane can be used to display the jaw and teeth in the same view.[1]

In tomosynthesis, projection images are acquired over a small angular range instead of the full 180° arc used in CT. It has been conventionally assumed that tomosynthesis reconstructions should only be created with planes parallel to the detector, since Fourier space is not sampled isotropically.[2] The sampling of Fourier space is determined from the Central Slice Theorem. As shown in Fig. 1 using a 2D parallel-beam geometry for illustration, the sampled region of Fourier space resembles a double cone whose opening angle matches the angular range of the tomosynthesis scan. This region is termed the "*Fourier double cone*" (FDC) throughout the remainder of this work, even though the region is not 3D in the strict sense of a cone.

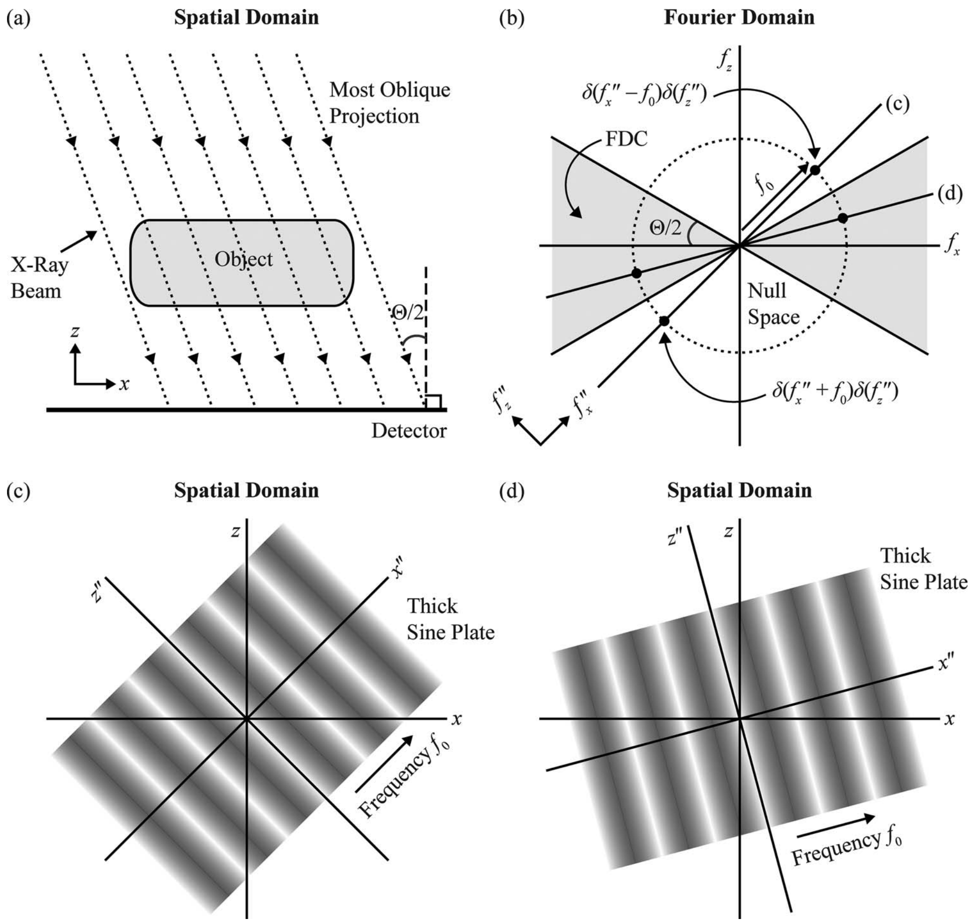

FIG. 1. (a) A parallel x-ray beam acquires a projection image for tomosynthesis. (b) According to the Central Slice Theorem, Fourier space is sampled along the direction perpendicular to the x-ray beam of each projection. Thus, the sampled area resembles a double cone whose opening angle matches the angular range (Θ) of the scan. This sampled area is termed the FDC in this work. (c) A test frequency is oriented along a pitch angle outside the FDC. Since the object is very thick, its Fourier transform consists of two delta functions along the pitch axis. This object is occult to tomosynthesis. (d) The same object is oriented along a pitch within the opening angle of the FDC. This object is sampled perfectly in Fourier space. Since a 0° pitch is always contained within the FDC, this thought experiment supports the use of conventional slices along a 0° pitch in the reconstruction of a thick object.

To gain insight into a reason for using reconstruction planes parallel to the detector, it is useful to perform a thought experiment with objects that are occult to tomosynthesis. Based on the Central Slice theorem, an object is occult to tomosynthesis if its Fourier transform is zero at all points inside the FDC. It can be demonstrated from standard properties concerning the Fourier transform that this condition is satisfied by a very thick object. Figure 1 illustrates this concept by considering a very thick object whose attenuation coefficient varies sinusoidally along an angle (i.e., "*pitch*"). The Fourier transform of the object consists of two delta functions along the pitch axis. One can use this object to assess whether individual frequencies are resolvable along various directions in the reconstruction. If one first considers the case in which the pitch is outside the opening angle of the FDC, it follows from the Central Slice Theorem that the reconstruction is zero everywhere [Fig. 1(c)]. Consequently, a slice that is reconstructed along the pitch of the object cannot resolve the input frequency. By contrast, if the same object has a pitch within the opening angle of the FDC, the test frequency is sampled perfectly in Fourier space [Fig. 1(d)]. By demonstrating that the object is resolved at pitches within the opening angle of the FDC, this thought experiment supports the use of conventional slices oriented along a 0° pitch. The 0° pitch is always contained within the opening angle of the FDC regardless of the angular range of the scanner.

It is now useful to investigate the effect of reducing the object thickness in the same thought experiment. As shown in Fig. 2, the Fourier transform of a thin sinusoidal object consists of two lines modulated by a "sinc" function along the direction perpendicular to the pitch axis. Because the Fourier transform has reasonably large modulation within the FDC, a slice along the pitch of the input frequency should not be trivial like the corresponding slice for a thick object.

To investigate whether an oblique reconstruction can indeed resolve a thin object, experimental images of a bar pattern phantom were acquired with a Selenia Dimensions digital breast tomosynthesis system (Hologic, Inc., Bedford, MA). A goniometry stand was used to vary the pitch of frequencies ranging from 1.0 to 10.0 line pairs per millimeter (lp/mm) in 1.0 lp/mm increments. The technique factors of the scan matched the ones given in our previous work.[3,4] Reconstruction was performed in the oblique plane of the bar patterns using a commercial prototype backprojection filtering (BPF)

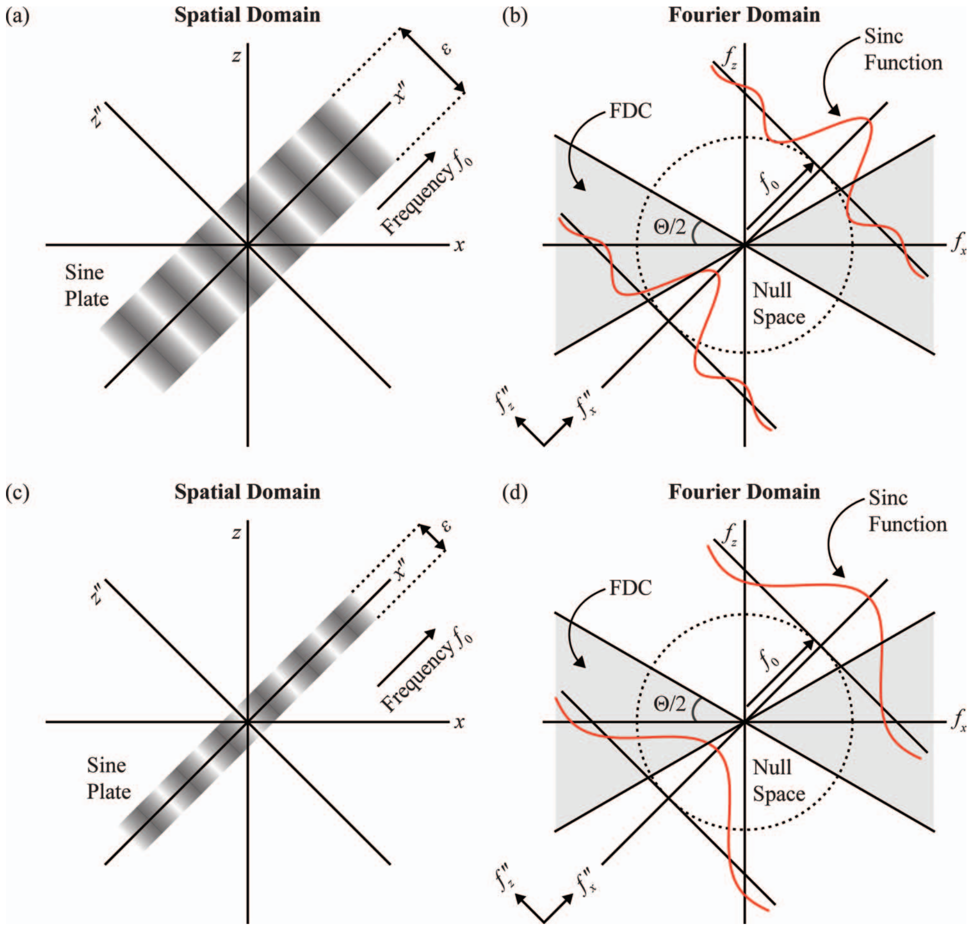

FIG. 2. To illustrate that a thin object can be visualized in an oblique reconstruction, a test frequency is analyzed at a nonzero pitch. As shown, the Fourier transform of the object consists of two lines modulated by a "sinc" function along the direction perpendicular to the pitch axis. Because the Fourier transform is nonzero within the FDC, a slice that is reconstructed along the pitch of the input frequency is expected to have information that would not otherwise be present for a thick object [Fig. 1(c)]. The amplitude of the portion of the "sinc" function that intersects the FDC increases as the object thickness is reduced; hence, the modulation in an oblique reconstruction is expected to be largest at small thicknesses.

algorithm (Briona™, Real Time Tomography, Villanova, PA).[5] Our previous work showed that frequencies up to 6.0 lp/mm can be resolved if the bar pattern phantom is parallel to the breast support (i.e., 0° pitch). Upon tilting the plane of the bar patterns, reconstructions showed that frequencies up to 5.0 and 3.0 lp/mm can be resolved at 30° and 60° pitches, respectively (Fig. 3). These experimental results indicate that slices in a tomosynthesis reconstruction do not have to be parallel to the breast support as stipulated by convention.

In breast tomosynthesis applications,[6–8] the objects in the American College of Radiology (ACR) Mammography Accreditation Phantom[9] give insight into the thickness of clinically important structures. One common attribute of all three objects in the ACR phantom (spheres, rods, and specks) is that they are thin. These objects are designed to simulate masses, spiculations, and calcifications, respectively, in breast images. The thickness of these objects is comparable to the bar pattern phantom considered in Fig. 3. For this reason, oblique reconstructions should have clinical applicability in tomosynthesis. Oblique reconstructions should allow a mammographer to determine the size of a mass more accurately in cases where the long axis of the lesion is pitched relative to the breast support. In addition, oblique reconstructions should improve the visualization of the structural morphology of spiculations and calcifications.

Although the experimental results indicate that thin objects can be resolved in oblique reconstructions, they also demonstrate that high frequency information is lost as the pitch is increased from 0°. The purpose of this paper is to develop an analytical model of image quality that offers deeper insight into these experimental results. Zhao developed a preliminary model of image quality for tomosynthesis by using linear systems theory to calculate the modulation transfer function (MTF).[2] Simplifying assumptions were made in that work in order to keep the mathematics tractable. Zhao assumed that slices in the reconstruction are parallel to the detector. In addition, Zhao did not model the effect of object thickness on MTF. In order to generalize Zhao's model, this paper calculates the MTF from first principles based on the relative signal of a sine plate at various frequencies. The limitations of Zhao's model are addressed by orienting the sine plate along various pitches and by analyzing the effect of object thickness. This paper provides a platform for determining the highest frequency that can be resolved in an oblique reconstruction for various object thicknesses.

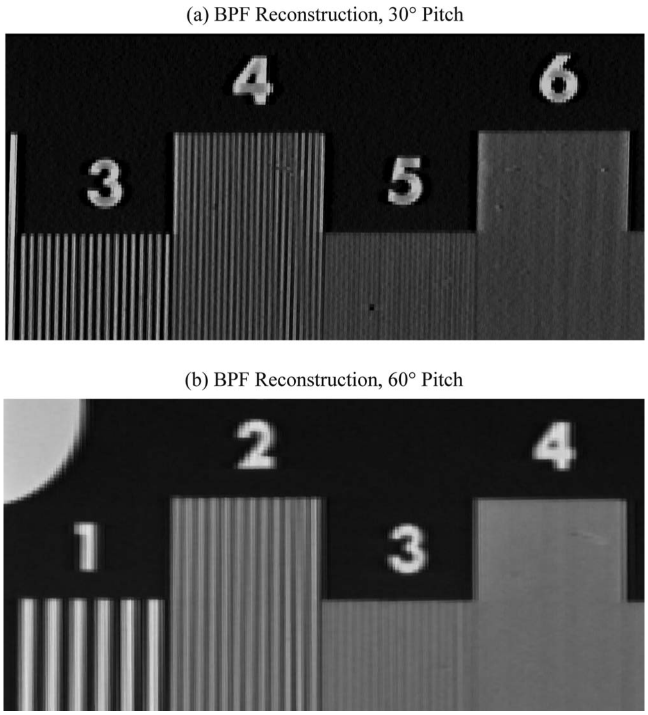

FIG. 3. To investigate the experimental feasibility of oblique reconstructions in a commercial breast tomosynthesis system, a bar pattern phantom was oriented along various pitches using a goniometry stand. The frequencies were pitched at 30° and 60° angles relative to the breast support. BPF reconstructions in the oblique plane of the bar patterns show frequencies up to 5.0 lp/mm and 3.0 lp/mm at the two respective pitches.

A second test object that is simulated in this paper is a pitched rod. This object is used to assess whether the length of an object can be correctly estimated along various directions in the reconstruction. Similar to the MTF, the accuracy of the length estimate is investigated as a function of the thickness of the object.

2. METHODS

2.A. Reconstruction formula for incomplete angular data

From first principles, a general filtered backprojection (FBP) reconstruction formula is now derived for an idealized tomosynthesis system with a parallel-beam geometry. This formula will be used to calculate the reconstruction of a pitched sine plate and a rod. Although clinical features are 3D, a 2D simulation is developed for a proof-of-principle justification for oblique reconstructions in tomosynthesis. In Paper II of this series of papers, the model of the reconstruction will be generalized to a broader set of assumptions which include a pixelated detector and a 3D acquisition geometry. Generalizing the model will allow us to investigate more advanced concepts that are beyond the scope of this paper, such as the spatial anisotropy of image quality in the reconstruction.

It is useful to begin this derivation with a review of the Radon transform. In a parallel-beam geometry, the Radon transform is defined by considering the integral of the linear attenuation coefficient of an object over all possible lines $\mathcal{L}(t,\theta)$ in $\mathbb{R}^2$. As shown in Fig. 4, $\mathcal{L}(t,\theta)$ denotes the line that passes through the point $(t\cos\theta,\, t\sin\theta)$ and that is perpendicular to the unit vector $\mathbf{p} = (\cos\theta)\mathbf{i} + (\sin\theta)\mathbf{k}$, where $\mathbf{i}$ and $\mathbf{k}$ are unit vectors in the x and z directions, respectively, and where $-\infty < t < \infty$ and $-90° < \theta \leq 90°$. Following Hsieh[10] and others, the matrix transformation

$$\begin{pmatrix} x \\ z \end{pmatrix} = \begin{pmatrix} \cos\theta & -\sin\theta \\ \sin\theta & \cos\theta \end{pmatrix} \begin{pmatrix} t \\ s \end{pmatrix} \tag{1}$$

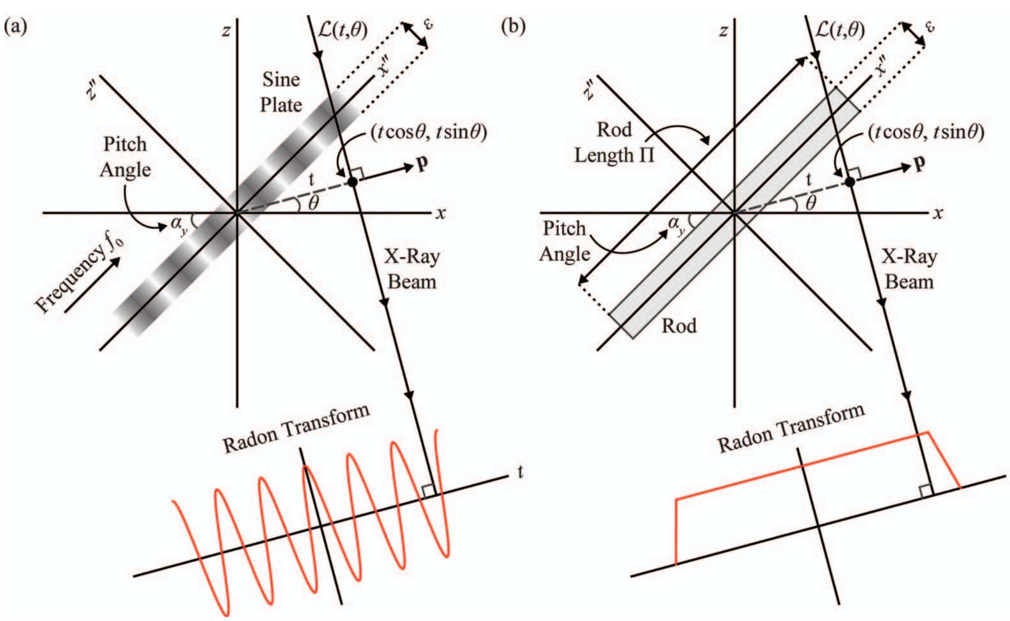

FIG. 4. In a parallel-beam geometry, the Radon transform is defined as the integral of an attenuation coefficient over the line $\mathcal{L}(t,\theta)$. This line intercepts the point $(t\cos\theta,\, t\sin\theta)$ and is perpendicular to the unit vector $\mathbf{p} = (\cos\theta)\mathbf{i} + (\sin\theta)\mathbf{k}$. At a fixed projection angle θ, the dependency of the Radon transform on the parameter t is illustrated for two test objects. (a) The first object is an infinitely long rectangular prism (thickness ε) whose attenuation coefficient varies sinusoidally along the pitch angle, α_y. (b) The second object is a rod (length Π) that is similarly pitched.

provides a parametric representation of the line $\mathcal{L}(t,\theta)$, assuming that (x, z) is a point in $\mathbb{R}^2$ and that s is a free parameter ranging from $-\infty$ to ∞. Denoting μ as the linear attenuation coefficient of the input object, the Radon transform can thus be written

$$\mathcal{R}\mu(t,\theta) = \int\limits_{\mathcal{L}(t,\theta)} \mu ds. \tag{2}$$

A fundamental relationship between the 1D Fourier transform of $\mathcal{R}\mu(t,\theta)$ and the 2D Fourier transform of $\mu(x, z)$ is established by the Central Slice Theorem[10,11]

$$\mathcal{F}_1(\mathcal{R}\mu)(f_r,\theta) = \mathcal{F}_2\mu(f_r\cos\theta,\ f_r\sin\theta), \tag{3}$$

where f_r is radial frequency ranging from $-\infty$ to ∞. According to Eq. (3), each projection samples Fourier space along the angle θ perpendicular to the incident x-ray beam. In tomosynthesis applications for which projections are acquired over a limited angular range, Fig. 1(b) shows the corresponding region of Fourier space that is sampled. This region has been termed the FDC in Sec. 1.

The Central Slice Theorem is now used to derive a formula for the FBP reconstruction of an object in a DBT system with incomplete angular data ranging from $\theta = -\Theta/2$ to $\theta = +\Theta/2$. For the purpose of this derivation, the system is taken to be noiseless and the angular spacing between projections is infinitesimally small. The FBP reconstruction[11] of $\mu(x, z)$ is

$$\mu_{\mathrm{FBP}}(x,z) = \int_{-\Theta/2}^{\Theta/2} (\phi *_1 \mathcal{R}\mu)(x\cos\theta + z\sin\theta,\theta)d\theta \tag{4}$$

$$= \int_{-\Theta/2}^{\Theta/2}\int_{-\infty}^{\infty} \phi(x\cos\theta + z\sin\theta - \tau) \cdot \mathcal{R}\mu(\tau,\theta)d\tau d\theta, \tag{5}$$

where ϕ is the filter and $*_1$ is the 1D convolution operator. Backprojection of $\mathcal{R}\mu(t,\theta)$ to the point (x, z) corresponds to evaluation of the Radon transform at $t = x\cos\theta + z\sin\theta$, as can be deduced from the inverse of the matrix transformation in Eq. (1). The transition from Eq. (4) to Eq. (5) follows directly from the definition of convolution. The 2D Fourier transform[12] of $\mu_{\mathrm{FBP}}(x, z)$ is thus

$$\mathcal{F}_2\mu_{\mathrm{FBP}}(f_r\cos\zeta,\ f_r\sin\zeta) = \int_{-\infty}^{\infty}\int_{-\infty}^{\infty}\int_{-\Theta/2}^{\Theta/2}\int_{-\infty}^{\infty} \phi(x\cos\theta + z\sin\theta - \tau) \cdot \mathcal{R}\mu(\tau,\theta)\cdot e^{-2\pi i f_r(x\cos\zeta + z\sin\zeta)}d\tau d\theta dx dz, \tag{6}$$

where ζ is the polar angle of the 2D frequency vector $(-90^\circ < \zeta \le 90^\circ)$. Equation (6) can be evaluated by changing variables from the (x, z) coordinate system to the (t, s) coordinate system. The differential area element $dxdz$ in Eq. (6) should be replaced by $dsdt$, since the Jacobian of the coordinate transformation in Eq. (1) is unity:

$$\mathcal{F}_2\mu_{\mathrm{FBP}}(f_r\cos\zeta,\ f_r\sin\zeta) = \int_{-\Theta/2}^{\Theta/2}\int_{-\infty}^{\infty} \mathcal{R}\mu(\tau,\theta) \cdot \left(\int_{-\infty}^{\infty}\phi(t-\tau)\cdot e^{-2\pi i f_r,t\cos(\theta-\zeta)}dt\right) \cdot \left(\int_{-\infty}^{\infty} e^{2\pi i f_r,s\sin(\theta-\zeta)}ds\right)d\tau d\theta. \tag{7}$$

In Eq. (7), the integral over t can be calculated using the Fourier shift theorem[12]

$$\int_{-\infty}^{\infty}\phi(t-\tau)\cdot e^{-2\pi i f_r t\cos(\theta-\zeta)}dt = e^{-2\pi i f_r\tau\cos(\theta-\zeta)}\cdot\mathcal{F}_1\phi[f_r\cos(\theta-\zeta)], \tag{8}$$

and the integral over s can be written in terms of a Dirac delta function:[13]

$$\int_{-\infty}^{\infty} e^{2\pi i f_r s\sin(\theta-\zeta)}ds = \delta[f_r\sin(\theta-\zeta)]. \tag{9}$$

Equation (9) can be simplified further by noting the composition identity for delta functions.[13,14] Assuming that $u(\theta)$ is a function with a finite number of zeros and with no repeated zeros, the identity for the delta function of a composition is

$$\delta\,[u(\theta)] = \sum_k \frac{\delta(\theta-\theta_{0k})}{|u'(\theta_{0k})|}, \tag{10}$$

where θ_{0k} is the kth zero of $u(\theta)$. In evaluating Eq. (9), we let $u(\theta) = f_r\sin(\theta-\zeta)$ and hence $\theta_{0k} = k\pi + \zeta$, where $k \in \mathbb{Z}$. Because the only zero of $u(\theta)$ that falls within the integration limits on θ in Eq. (7) is θ_{00}, the summation in Eq. (10) reduces to the single term for which $k = 0$. Noting that $u'(\theta) = f_r\cos(\theta-\zeta)$, it follows that $u'(\theta_{00}) = f_r$ and Eq. (9) simplifies to

$$\delta[f_r\sin(\theta-\zeta)] = \frac{\delta(\theta-\zeta)}{|f_r|}. \tag{11}$$

Combining Eqs. (7)–(11), the 2D Fourier transform of $\mu_{\mathrm{FBP}}(x, z)$ can now be written as

$$\mathcal{F}_2\mu_{\mathrm{FBP}}(f_r\cos\zeta,\ f_r\sin\zeta) = \int_{-\Theta/2}^{\Theta/2}\left(\int_{-\infty}^{\infty}\mathcal{R}\mu(\tau,\theta)\cdot e^{-2\pi i f_r\tau\cos(\theta-\zeta)}d\tau\right) \cdot\mathcal{F}_1\phi[f_r\cos(\theta-\zeta)]\cdot\frac{\delta(\theta-\zeta)}{|f_r|}d\theta. \tag{12}$$

In Eq. (12), the integral over τ can be evaluated using the Central Slice theorem [Eq. (3)]:

$$\mathcal{F}_2\mu_{\mathrm{FBP}}(f_r\cos\zeta,\ f_r\sin\zeta) = \int_{-\Theta/2}^{\Theta/2}\mathcal{F}_2\mu[f_r\cos(\theta-\zeta)\cos\theta,\ f_r\cos(\theta-\zeta)\sin\theta] \cdot\mathcal{F}_1\phi[f_r\cos(\theta-\zeta)]\cdot\frac{\delta(\theta-\zeta)}{|f_r|}d\theta. \tag{13}$$

Due to the delta function in Eq. (13), this integration is nontrivial only if ζ is between $-\Theta/2$ and $+\Theta/2$; otherwise, the integral vanishes. For this reason, it is important to introduce the function $\mathrm{rect}(\zeta/\Theta)$ in the evaluation of Eq. (13), so that

$$\mathcal{F}_2\mu_{\mathrm{FBP}}(f_r\cos\zeta,\ f_r\sin\zeta) = \frac{1}{|f_r|}\cdot\mathcal{F}_2\mu(f_r\cos\zeta,\ f_r\sin\zeta) \cdot\mathcal{F}_1\phi(f_r)\cdot\mathrm{rect}\left(\frac{\zeta}{\Theta}\right), \tag{14}$$

where

$$\mathrm{rect}(u) \equiv \begin{cases} 1, & |u| \le 1/2 \\ 0, & |u| > 1/2 \end{cases}. \quad (15)$$

In Eq. (14), the function $\mathrm{rect}(\zeta/\Theta)$ perfectly recovers the FDC whose opening angle is the scan range Θ (Fig. 1). This result completes the derivation of the general tomosynthesis reconstruction formula.

If one considers the case of complete angular data ($\Theta = 180°$), all of Fourier space is sampled by the projections, and the rectangle function in Eq. (14) can be replaced with a constant (unity). By choosing the filter ϕ with the property that $\mathcal{F}_1\phi(f_r) = |f_r|$, it follows directly from Eq. (14) that the input object can be reconstructed perfectly. This formula for ϕ is termed the "ramp" filter; it has been previously derived by Hsieh[10] and others for CT applications with complete angular data. This agreement with CT reconstruction theory provides a built-in check on the validity of Eq. (14).

With incomplete angular data ($0 < \Theta < 180°$), it is no longer possible to choose a filter ϕ such that there is always agreement between $\mathcal{F}_2\mu_{\mathrm{FBP}}$ and $\mathcal{F}_2\mu$ in Eq. (14). In Secs. 2.B and 2.C of this paper, Eq. (14) is used to calculate the reconstruction of a pitched sine plate and rod in tomosynthesis applications with incomplete angular data.

In determining the reconstruction of the two test objects, an important property to simplify calculations is that the spatial representation of the reconstruction is real-valued. Following the convolution theorem, the spatial representation is

$$\mu_{\mathrm{FBP}}(x, z) = \mu(x, z) *_2 \mathcal{F}_2^{-1}\left[\frac{1}{|f_r|} \cdot \mathcal{F}_1\phi(f_r) \cdot \mathrm{rect}\left(\frac{\zeta}{\Theta}\right)\right](x, z) \quad (16)$$

where $*_2$ denotes the 2D convolution operator. From standard properties, the 2D inverse Fourier transform to the right of the convolution operator must be real-valued if the argument in the rectangular brackets is an even function. Since $1/|f_r|$ and $\mathrm{rect}(\zeta/\Theta)$ are even functions, it follows that the reconstruction is real-valued provided that $\mathcal{F}_1\phi(f_r)$ is also even. This work is limited to filters that are even functions in Fourier space. Two examples of filters that satisfy this property are the ramp filter and the Hanning window function.[2–4,15] In breast tomosynthesis applications, the ramp filter is used to reduce the low frequency detector response, while the Hanning window function is used to suppress high frequency noise.

2.B. Reconstruction of a pitched sine plate

A framework for investigating the reconstruction of a sine plate is now developed by modeling an infinitely long rectangular prism whose attenuation coefficient varies sinusoidally along the pitch α_y. To illustrate that reconstructions are feasible along a broad range of pitches, the angle α_y is taken to be larger than $\Theta/2$, so that the pitch is outside the opening angle of the FDC (Fig. 1):

$$\mu(x'', z'') = C \cdot \cos(2\pi f_0 x'') \cdot \mathrm{rect}\left(\frac{z''}{\varepsilon}\right), \quad (17)$$

where

$$\begin{pmatrix} x'' \\ z'' \end{pmatrix} = \begin{pmatrix} \cos\alpha_y & \sin\alpha_y \\ -\sin\alpha_y & \cos\alpha_y \end{pmatrix}\begin{pmatrix} x \\ z \end{pmatrix}. \quad (18)$$

In this formulation, C denotes the maximum value of the attenuation coefficient of the material, f_0 is the input frequency, x'' indicates position along the pitch α_y, and z'' measures position along the thickness (ε) of the sine plate [Fig. 4(a)]. The transformation matrix given in Eq. (18) changes variables between the (x, z) coordinate system and a rotated reference frame whose coordinate axes match the long and short axes of the pitched sine plate, respectively. The subscript y on the variable α_y emphasizes that changing the pitch is equivalent to rotating the x and z axes about the y axis perpendicular to the plane of the parallel projections. For the purpose of this work, it is assumed that $0 \le \alpha_y \le 90°$.

To illustrate the calculation of $\mathcal{R}\mu(t, \theta)$, the Radon transform of this object is plotted versus t in Fig. 4(a) at a fixed projection angle (θ). Appendix A demonstrates from first principles that this plot is sinusoidal with frequency $f_0 \sec(\theta - \alpha_y)$, as shown in the figure.

To calculate the tomosynthesis reconstruction of the sine plate [Eq. (14)], it is first necessary to determine the Fourier transform of the sine plate

$$\mathcal{F}_2\mu(f_x, f_z) \equiv \int_{-\infty}^{\infty}\int_{-\infty}^{\infty} \mu(x, z) e^{-2\pi i(f_x x + f_z z)} dx dz, \quad (19)$$

$$= \int_{-\infty}^{\infty}\int_{-\infty}^{\infty} \mu(x'', z'') e^{-2\pi i(f_x'' x'' + f_z'' z'')} dx'' dz''. \quad (20)$$

In Eq. (20), the frequency variables (f_x'', f_z'') are defined by a rotated reference frame analogous to the (x'', z'') coordinate system

$$\begin{pmatrix} f_x'' \\ f_z'' \end{pmatrix} = \begin{pmatrix} \cos\alpha_y & \sin\alpha_y \\ -\sin\alpha_y & \cos\alpha_y \end{pmatrix}\begin{pmatrix} f_x \\ f_z \end{pmatrix}. \quad (21)$$

Substituting Eq. (17) into Eq. (20) yields

$$\mathcal{F}_2\mu(f_x'', f_z'') = \frac{C\varepsilon}{2}[\delta(f_x'' - f_0) + \delta(f_x'' + f_0)]\mathrm{sinc}(\varepsilon f_z''), \quad (22)$$

where

$$\mathrm{sinc}(u) \equiv \frac{\sin(\pi u)}{\pi u}. \quad (23)$$

Using Eq. (22) in conjunction with Eq. (14), the FBP reconstruction can now be written as the inverse 2D Fourier transform

$$\mu_{\mathrm{FBP}} = \int_{-\infty}^{\infty}\int_{-\infty}^{\infty} \frac{\mathcal{F}_2\mu}{\sqrt{f_x^2 + f_z^2}} \cdot \mathcal{F}_1\phi(f_r) \cdot \mathrm{rect}\left(\frac{\zeta}{\Theta}\right) \cdot e^{2\pi i(x f_x + z f_z)} df_x df_z \quad (24)$$

$$= \int_{-\infty}^{\infty}\int_{-\infty}^{\infty} \frac{\mathcal{F}_2\mu}{\sqrt{f_x^2 + f_z^2}} \cdot \mathcal{F}_1\phi\,(|f_r|) \cdot \mathrm{rect}\left(\frac{\zeta}{\Theta}\right) \cdot \cos[2\pi(x f_x + z f_z)] df_x df_z. \quad (25)$$

The transition from Eq. (24) to Eq. (25) is justified from *a priori* knowledge that the reconstruction is real-valued. Equation (25) can now be evaluated by changing variables into the (f_x'', f_z'') and (x'', z'') coordinate systems. Combining Eqs. (18), (21), (22), and (25) gives

$$\mu_{\mathrm{FBP}} = \frac{C\varepsilon}{2}\int_{-\infty}^{\infty}\int_{-\infty}^{\infty}\delta(f_x''+f_0)\cdot\mathcal{F}_1\phi(|f_r|)\cdot\mathrm{rect}\left(\frac{\zeta}{\Theta}\right)\cdot\frac{\cos[2\pi(x''f_x''+z''f_z'')]\mathrm{sinc}(\varepsilon f_z'')}{\sqrt{f_x''^2+f_z''^2}}df_x''df_z''$$
$$+\frac{C\varepsilon}{2}\int_{-\infty}^{\infty}\int_{-\infty}^{\infty}\delta(f_x''-f_0)\cdot\mathcal{F}_1\phi(|f_r|)\cdot\mathrm{rect}\left(\frac{\zeta}{\Theta}\right)\cdot\frac{\cos[2\pi(x''f_x''+z''f_z'')]\mathrm{sinc}(\varepsilon f_z'')}{\sqrt{f_x''^2+f_z''^2}}df_x''df_z''. \quad (26)$$

In evaluating this expression, the inner integrals over f_x'' can be simplified by substituting the constraints $f_x'' = -f_0$ and $f_x'' = +f_0$ into the terms to the right of the delta function in each respective integrand. This step follows directly from the definition of the delta function. Because of the term rect(ζ/Θ), the outer integral over f_z'' must then be evaluated along integration limits given from the intersection of the FDC with the lines $f_x'' = \pm f_0$. Figure 5(a) shows a pitch for which this intersection consists of two line segments. At larger pitches approaching 90°, the intersection consists of infinitely long rays [Fig. 5(b)]. FBP reconstruction is now calculated separately for these two cases.

2.B.1. *Case 1*

Figure 5(a) illustrates a pitch for which the FDC intersects the lines $f_x'' = \pm f_0$ along two line segments. The coordinates of the two lines segments are now derived. It is shown in Fig. 5(a) that, along the line $f_x'' = -f_0$, the first line segment lies along the f_z'' direction with extent between $|\overrightarrow{\mathrm{PQ}}|$ and $|\overrightarrow{\mathrm{PR}}|$. In applying trigonometry to the right triangle OPQ, it follows that

$$|\overrightarrow{\mathrm{PQ}}| = |\overrightarrow{\mathrm{OP}}|\cdot\tan(\alpha_y-\Theta/2), \quad (27)$$

$$= f_0\tan(\alpha_y-\Theta/2). \quad (28)$$

Similarly, in considering the right triangle OPR,

$$|\overrightarrow{\mathrm{PR}}| = |\overrightarrow{\mathrm{OP}}|\cdot\tan(\alpha_y+\Theta/2), \quad (29)$$

$$= f_0\tan(\alpha_y+\Theta/2). \quad (30)$$

In Eq. (30), the tangent function tends to infinity if $\alpha_y = 90^\circ - \Theta/2$. For this reason, if the pitch falls between the limits $90^\circ - \Theta/2 < \alpha_y < 90^\circ$, it is no longer true that the FDC intersects the lines $f_x'' = \pm f_0$ along line segments. Instead, the intersection consists of infinitely long rays. This case is considered in Sec. 2.B.2. To simplify Eqs. (28) and (30), one can introduce the term $\nu_\pm$

$$\nu_\pm \equiv f_0\tan(\alpha_y\pm\Theta/2), \quad (31)$$

so that Eq. (26) can be evaluated as

$$\mu_{\mathrm{FBP}} = \frac{C\varepsilon}{2}\left[\int_{\nu_-}^{\nu_+}\frac{\mathcal{F}_1\phi\left(\sqrt{f_0^2+f_z''^2}\right)\cos\left[2\pi(-x''f_0+z''f_z'')\right]\mathrm{sinc}(\varepsilon f_z'')}{\sqrt{f_0^2+f_z''^2}}df_z'' + \int_{-\nu_+}^{-\nu_-}\frac{\mathcal{F}_1\phi\left(\sqrt{f_0^2+f_z''^2}\right)\cos\left[2\pi(x''f_0+z''f_z'')\right]\mathrm{sinc}(\varepsilon f_z'')}{\sqrt{f_0^2+f_z''^2}}df_z''\right] \quad (32)$$

$$= \frac{C\varepsilon}{2}\left[\begin{array}{l}\cos(2\pi x''f_0)\left(\int_{\nu_-}^{\nu_+}\frac{\mathcal{F}_1\phi\left(\sqrt{f_0^2+f_z''^2}\right)\cos(2\pi z''f_z'')\mathrm{sinc}(\varepsilon f_z'')}{\sqrt{f_0^2+f_z''^2}}df_z'' + \int_{-\nu_+}^{-\nu_-}\frac{\mathcal{F}_1\phi\left(\sqrt{f_0^2+f_z''^2}\right)\cos(2\pi z''f_z'')\mathrm{sinc}(\varepsilon f_z'')}{\sqrt{f_0^2+f_z''^2}}df_z''\right)\\ +\sin(2\pi x''f_0)\left(\int_{\nu_-}^{\nu_+}\frac{\mathcal{F}_1\phi\left(\sqrt{f_0^2+f_z''^2}\right)\sin(2\pi z''f_z'')\mathrm{sinc}(\varepsilon f_z'')}{\sqrt{f_0^2+f_z''^2}}df_z'' - \int_{-\nu_+}^{-\nu_-}\frac{\mathcal{F}_1\phi\left(\sqrt{f_0^2+f_z''^2}\right)\sin(2\pi z''f_z'')\mathrm{sinc}(\varepsilon f_z'')}{\sqrt{f_0^2+f_z''^2}}df_z''\right)\end{array}\right]. \quad (33)$$

In deriving Eq. (32), a symmetry property has been used to determine the integration limits along the line $f_x'' = +f_0$ from knowledge of the analogous limits along the line $f_x'' = -f_0$. The transition from Eq. (32) to (33) is justified by the angle-sum

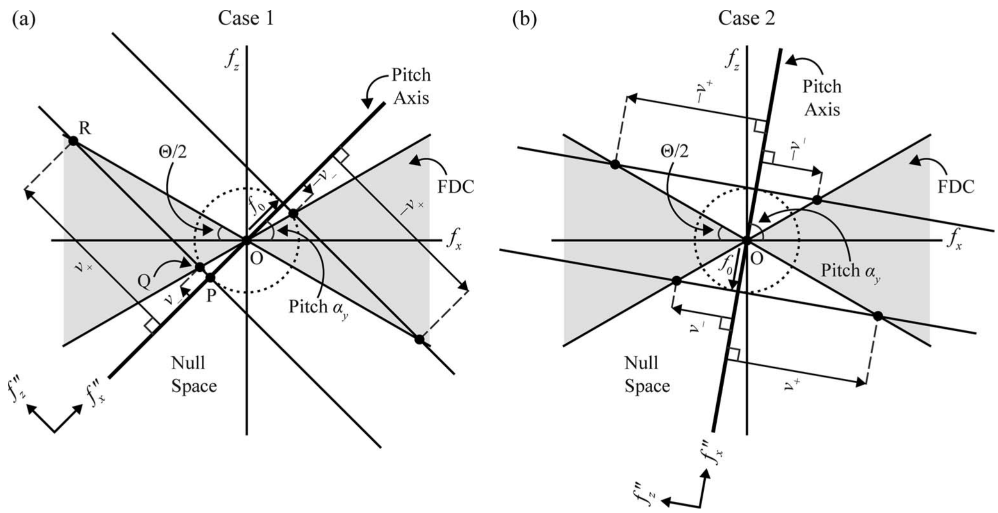

FIG. 5. (a) By rotating the coordinate axes of Fourier space by the pitch of the test object, it can be shown that the Fourier transform of a sine plate with frequency f_0 [Fig. 4(a)] consists of the two lines $f''_x = \pm f_0$. As shown, these lines intersect the FDC along two line segments. This property holds if $0 \le \alpha_y < 90^\circ - \Theta/2$. (b) At larger pitches for which $90^\circ - \Theta/2 < \alpha_y \le 90^\circ$, it can be demonstrated that the Fourier transform of the sine plate intersects the FDC along four rays.

identity

$$\cos(b_1 + b_2) = \cos(b_1)\cos(b_2) - \sin(b_1)\sin(b_2) \tag{34}$$

for the real numbers b_1 and b_2. Equation (33) can now be simplified by noting that that the first and second integrals are equivalent, despite the different integration limits. This result holds because the integrands are an even function of f''_z, and the two integration intervals are at equivalent distances from $f''_z = 0$. It can also be shown that the third and fourth integrals in Eq. (33) have the same magnitude but opposite sign. This claim follows from the fact that each integrand is an odd function of f''_z, and the two integration intervals are at the same distance from $f''_z = 0$. The negative sign preceding the fourth integral yields net equivalence with the third integral, so that

$$\mu_{\mathrm{FBP}} = C\varepsilon \left[\cos(2\pi x'' f_0) \int_{\nu_-}^{\nu_+} \frac{\mathcal{F}_1\phi\left(\sqrt{f_0^2 + f_z''^2}\right)\cos(2\pi z'' f''_z)\mathrm{sinc}(\varepsilon f''_z)}{\sqrt{f_0^2 + f_z''^2}} df''_z \right.$$
$$\left. + \sin(2\pi x'' f_0) \int_{\nu_-}^{\nu_+} \frac{\mathcal{F}_1\phi\left(\sqrt{f_0^2 + f_z''^2}\right)\sin(2\pi z'' f''_z)\mathrm{sinc}(\varepsilon f''_z)}{\sqrt{f_0^2 + f_z''^2}} df''_z \right]. \tag{35}$$

It would be difficult to evaluate the two integrals analytically in Eq. (35). Instead, they can be determined numerically using the midpoint formula for integration[16]

$$\mu_{\mathrm{FBP}} \cong C\varepsilon(\nu_+ - \nu_-) \cdot \lim_{J\to\infty} \frac{1}{J} \left[\begin{array}{l} \cos(2\pi x'' f_0) \displaystyle\sum_{j=1}^{J} \frac{\mathcal{F}_1\phi\left(\sqrt{f_0^2 + f_{zj}''^2}\right)\cos(2\pi z'' f''_{zj})\mathrm{sinc}(\varepsilon f''_{zj})}{\sqrt{f_0^2 + f_{zj}''^2}} \\ + \sin(2\pi x'' f_0) \displaystyle\sum_{j=1}^{J} \frac{\mathcal{F}_1\phi\left(\sqrt{f_0^2 + f_{zj}''^2}\right)\sin(2\pi z'' f''_{zj})\mathrm{sinc}(\varepsilon f''_{zj})}{\sqrt{f_0^2 + f_{zj}''^2}} \end{array} \right]. \tag{36}$$

In applying the midpoint formula to Eq. (35), the interval $[\nu_-, \nu_+]$, which corresponds to the integration limits, is evenly partitioned into subintervals. The midpoint of the jth subinterval is

$$f''_{zj} \equiv \nu_- + \frac{(j - 1/2)(\nu_+ - \nu_-)}{J}, \tag{37}$$

where J is the total number of subintervals ($J \to \infty$). The midpoint formula is a valid approximation method provided that the integration limits are finite. This property holds if $0^\circ \le \alpha_y < 90^\circ - \Theta/2$.

2.B.2. Case 2

In Sec. 2.B.1, it was demonstrated that the FDC intersects the lines $f_x'' = \pm f_0$ along infinitely long rays if the pitch satisfies the inequality $90^\circ - \Theta/2 < \alpha_y \leq 90^\circ$. Figure 5(b) shows the four rays of intersection. It follows that

$$\mu_{\mathrm{FBP}} = \frac{C\varepsilon}{2}\left[\begin{array}{l} \displaystyle\int_{-\infty}^{\nu_+} \frac{\mathcal{F}_1\phi\left(\sqrt{f_0^2+f_z''^2}\right)\cos\left[2\pi(-x''f_0+z''f_z'')\right]\mathrm{sinc}(\varepsilon f_z'')}{\sqrt{f_0^2+f_z''^2}}df_z'' \\ \displaystyle+\int_{\nu_-}^{\infty} \frac{\mathcal{F}_1\phi\left(\sqrt{f_0^2+f_z''^2}\right)\cos\left[2\pi(-x''f_0+z''f_z'')\right]\mathrm{sinc}(\varepsilon f_z'')}{\sqrt{f_0^2+f_z''^2}}df_z'' \\ \displaystyle+\int_{-\infty}^{-\nu_-} \frac{\mathcal{F}_1\phi\left(\sqrt{f_0^2+f_z''^2}\right)\cos\left[2\pi(x''f_0+z''f_z'')\right]\mathrm{sinc}(\varepsilon f_z'')}{\sqrt{f_0^2+f_z''^2}}df_z'' \\ \displaystyle+\int_{-\nu_+}^{\infty} \frac{\mathcal{F}_1\phi\left(\sqrt{f_0^2+f_z''^2}\right)\cos\left[2\pi(x''f_0+z''f_z'')\right]\mathrm{sinc}(\varepsilon f_z'')}{\sqrt{f_0^2+f_z''^2}}df_z'' \end{array}\right] \quad (38)$$

$$= C\varepsilon\left[\begin{array}{l} \displaystyle\cos(2\pi x''f_0)\left(\int_{-\infty}^{\nu_+} \frac{\mathcal{F}_1\phi\left(\sqrt{f_0^2+f_z''^2}\right)\cos(2\pi z''f_z'')\mathrm{sinc}(\varepsilon f_z'')}{\sqrt{f_0^2+f_z''^2}}df_z'' \right.\\ \displaystyle\left.+\int_{\nu_-}^{\infty} \frac{\mathcal{F}_1\phi\left(\sqrt{f_0^2+f_z''^2}\right)\cos(2\pi z''f_z'')\mathrm{sinc}(\varepsilon f_z'')}{\sqrt{f_0^2+f_z''^2}}df_z''\right) \\ \displaystyle+\sin(2\pi x''f_0)\left(\int_{-\infty}^{\nu_+} \frac{\mathcal{F}_1\phi\left(\sqrt{f_0^2+f_z''^2}\right)\sin(2\pi z''f_z'')\mathrm{sinc}(\varepsilon f_z'')}{\sqrt{f_0^2+f_z''^2}}df_z'' \right.\\ \displaystyle\left.+\int_{\nu_-}^{\infty} \frac{\mathcal{F}_1\phi\left(\sqrt{f_0^2+f_z''^2}\right)\sin(2\pi z''f_z'')\mathrm{sinc}(\varepsilon f_z'')}{\sqrt{f_0^2+f_z''^2}}df_z''\right) \end{array}\right]. \quad (39)$$

One can justify the transition from Eq. (38) to (39) by applying steps analogous to the ones used between Eqs. (32) and (35). Since the integration limits are not all finite, it is no longer acceptable to evaluate these integrals with the midpoint formula. For the purpose of this work, the integrals are evaluated numerically in MATLAB R2012b using the "integral" command.

2.C. Reconstruction of a pitched rod

The reconstruction of a pitched rod is now determined by modifying the attenuation coefficient of the input object in Eq. (17). The rod is modeled as a rectangle function with length (Π) aligned along the pitch α_y [Fig. 4(b)]:

$$\mu(x'', z'') = C \cdot \mathrm{rect}\left(\frac{x''}{\Pi}\right) \cdot \mathrm{rect}\left(\frac{z''}{\varepsilon}\right). \quad (40)$$

Similar to the sine plate, the rod thickness is ε, and the maximum value of the attenuation coefficient is C. The pitch α_y is assumed to be larger than $\Theta/2$, so that the long axis of the rod is not within the opening angle of the FDC. To illustrate the Radon transform of this object, its dependency on t is shown in Fig. 4(b) at a fixed projection angle (θ). The Radon transform is calculated in Appendix B from first principles.

As discussed in Sec. 2.B, it is necessary to calculate the Fourier transform of the input object in order to derive the reconstruction. Following Eq. (20), this transform can be written

$$\mathcal{F}_2\mu(f_x'', f_z'') = C\Pi\varepsilon \cdot \mathrm{sinc}(\Pi f_x'')\mathrm{sinc}(\varepsilon f_z''). \quad (41)$$

The reconstruction can now be determined by substituting Eq. (41) into Eq. (25):

$$\mu_{\mathrm{FBP}}(x, z) = C\Pi\varepsilon\int_{-\infty}^{\infty}\int_{-\infty}^{\infty} \frac{\mathrm{sinc}(\Pi f_x'')\mathrm{sinc}(\varepsilon f_z'')}{\sqrt{f_x^2+f_z^2}} \cdot \mathcal{F}_1\phi\left(|f_r|\right) \cdot \mathrm{rect}\left(\frac{\zeta}{\Theta}\right) \cdot \cos\left[2\pi(xf_x+zf_z)\right] df_z df_x \quad (42)$$

$$= C\Pi\varepsilon \int_{-\infty}^{0} \int_{f_x \tan(\Theta/2)}^{-f_x \tan(\Theta/2)} \frac{\mathrm{sinc}[\Pi(f_x \cos\alpha_y + f_z \sin\alpha_y)]\mathrm{sinc}[\varepsilon(-f_x \sin\alpha_y + f_z \cos\alpha_y)]}{\sqrt{f_x^2 + f_z^2}} \mathcal{F}_1\phi(|f_r|)\cos[2\pi(xf_x + zf_z)]df_z df_x$$
$$+ C\Pi\varepsilon \int_{0}^{\infty} \int_{-f_x \tan(\Theta/2)}^{f_x \tan(\Theta/2)} \frac{\mathrm{sinc}[\Pi(f_x \cos\alpha_y + f_z \sin\alpha_y)]\mathrm{sinc}[\varepsilon(-f_x \sin\alpha_y + f_z \cos\alpha_y)]}{\sqrt{f_x^2 + f_z^2}} \mathcal{F}_1\phi(|f_r|)\cos[2\pi(xf_x + zf_z)]df_z df_x. \quad (43)$$

To transition from Eq. (42) to Eq. (43), the arguments of the sinc functions are transformed into the (f_x, f_z) coordinate system using Eq. (21). Also, the limits of the inner integral over f_z are modified to model the FDC. Because it would be difficult to evaluate the inner integrals over f_z in closed form, the midpoint formula[16] can now be used as an approximation technique. Similar to Eq. (35), the two intervals of integration in Eq. (43) should be evenly partitioned into subintervals numbered between $k = 1$ and K, so that

$$\mu_{\mathrm{FBP}}(x,z) = C\Pi\varepsilon \int_{-\infty}^{0} \lim_{K\to\infty} \frac{-2f_x \tan(\Theta/2)}{K} \sum_{k=1}^{K} \frac{\mathcal{F}_1\phi\left(\sqrt{f_x^2 + f_{zk}^2}\right) \mathrm{sinc}(\Upsilon_{1k}^{-} f_x)\mathrm{sinc}(\Upsilon_{2k}^{-} f_x)\cos(\pi\Upsilon_{3k}^{-} f_x)}{\sqrt{f_x^2 + f_{zk}^2}} df_x$$
$$+ C\Pi\varepsilon \int_{0}^{\infty} \lim_{K\to\infty} \frac{2f_x \tan(\Theta/2)}{K} \sum_{k=1}^{K} \frac{\mathcal{F}_1\phi\left(\sqrt{f_x^2 + f_{zk}^2}\right) \mathrm{sinc}(\Upsilon_{1k}^{+} f_x)\mathrm{sinc}(\Upsilon_{2k}^{+} f_x)\cos(\pi\Upsilon_{3k}^{+} f_x)}{\sqrt{f_x^2 + f_{zk}^2}} df_x, \quad (44)$$

where

$$f_{zk} \equiv 2f_x \tan\left(\frac{\Theta}{2}\right)\left[\frac{k-1/2}{K} - \frac{1}{2}\right], \quad (45)$$

$$\Upsilon_{1k}^{\pm} \equiv \Pi\left[\cos\alpha_y \pm 2\left(\frac{k-1/2}{K} - \frac{1}{2}\right)\tan\left(\frac{\Theta}{2}\right)\sin(\alpha_y)\right], \quad (46)$$

$$\Upsilon_{2k}^{\pm} \equiv \varepsilon\left[-\sin\alpha_y \pm 2\left(\frac{k-1/2}{K} - \frac{1}{2}\right)\tan\left(\frac{\Theta}{2}\right)\cos(\alpha_y)\right], \quad (47)$$

$$\Upsilon_{3k}^{\pm} \equiv 2\left[x \pm 2z\left(\frac{k-1/2}{K} - \frac{1}{2}\right)\tan\left(\frac{\Theta}{2}\right)\right]. \quad (48)$$

The integrals in Eq. (44) cannot be evaluated analytically for the most general filter ϕ. One special case that can be simplified, however, is simple backprojection (SBP) reconstruction for which $\mathcal{F}_1\phi(f_r) = 1$:

$$\mathcal{B}(\mathcal{R}\mu)(x,z) = C\Pi\varepsilon \int_{-\infty}^{0} \lim_{K\to\infty} \frac{-2f_x \tan(\Theta/2)}{K} \sum_{k=1}^{K} \frac{\mathrm{sinc}(\Upsilon_{1k}^{-} f_x)\mathrm{sinc}(\Upsilon_{2k}^{-} f_x)\cos(\pi\Upsilon_{3k}^{-} f_x)}{\sqrt{f_x^2\left(1 + 4\tan^2\left(\frac{\Theta}{2}\right)\left[\frac{k-1/2}{K} - \frac{1}{2}\right]^2\right)}} df_x$$
$$+ C\Pi\varepsilon \int_{0}^{\infty} \lim_{K\to\infty} \frac{2f_x \tan(\Theta/2)}{K} \sum_{k=1}^{K} \frac{\mathrm{sinc}(\Upsilon_{1k}^{+} f_x)\mathrm{sinc}(\Upsilon_{2k}^{+} f_x)\cos(\pi\Upsilon_{3k}^{+} f_x)}{\sqrt{f_x^2\left(1 + 4\tan^2\left(\frac{\Theta}{2}\right)\left[\frac{k-1/2}{K} - \frac{1}{2}\right]^2\right)}} df_x. \quad (49)$$

Since

$$\sqrt{f_x^2} = \begin{cases} -f_x, & f_x < 0 \\ +f_x, & f_x \geq 0 \end{cases}, \quad (50)$$

it follows that

$$\mathcal{B}(\mathcal{R}\mu)(x,z) = C\Pi\varepsilon \int_{-\infty}^{0} \lim_{K\to\infty} \frac{-2f_x \tan(\Theta/2)}{K} \sum_{k=1}^{K} \frac{\mathrm{sinc}(\Upsilon_{1k}^{-} f_x)\mathrm{sinc}(\Upsilon_{2k}^{-} f_x)\cos(\pi\Upsilon_{3k}^{-} f_x)}{(-f_x)\sqrt{1 + 4\tan^2\left(\frac{\Theta}{2}\right)\left[\frac{k-1/2}{K} - \frac{1}{2}\right]^2}} df_x$$
$$+ C\Pi\varepsilon \int_{0}^{\infty} \lim_{K\to\infty} \frac{2f_x \tan(\Theta/2)}{K} \sum_{k=1}^{K} \frac{\mathrm{sinc}(\Upsilon_{1k}^{+} f_x)\mathrm{sinc}(\Upsilon_{2k}^{+} f_x)\cos(\pi\Upsilon_{3k}^{+} f_x)}{(f_x)\sqrt{1 + 4\tan^2\left(\frac{\Theta}{2}\right)\left[\frac{k-1/2}{K} - \frac{1}{2}\right]^2}} df_x \quad (51)$$

$$= 2C\Pi\varepsilon\tan(\Theta/2)\cdot\lim_{K\to\infty}\sum_{k=1}^{K}\frac{I^{-}_{k,\mathrm{SBP}}+I^{+}_{k,\mathrm{SBP}}}{K\sqrt{1+4\tan^2\left(\frac{\Theta}{2}\right)\left[\frac{k-1/2}{K}-\frac{1}{2}\right]^2}},\tag{52}$$

where

$$I^{-}_{k,\mathrm{SBP}} = \int_{-\infty}^{0}\mathrm{sinc}(\Upsilon^{-}_{1k}f_x)\mathrm{sinc}(\Upsilon^{-}_{2k}f_x)\cos(\pi\Upsilon^{-}_{3k}f_x)df_x,\tag{53}$$

$$I^{+}_{k,\mathrm{SBP}} = \int_{0}^{\infty}\mathrm{sinc}(\Upsilon^{+}_{1k}f_x)\mathrm{sinc}(\Upsilon^{+}_{2k}f_x)\cos(\pi\Upsilon^{+}_{3k}f_x)df_x.\tag{54}$$

Using a computer algebra system (Maple 16, Maplesoft, Waterloo, Ontario) to evaluate Eqs. (53) and (54), it can be shown that

$$I^{\pm}_{k,\mathrm{SBP}} = \frac{\left|\Upsilon^{\pm}_{1k}+\Upsilon^{\pm}_{2k}+\Upsilon^{\pm}_{3k}\right|+\left|\Upsilon^{\pm}_{1k}+\Upsilon^{\pm}_{2k}-\Upsilon^{\pm}_{3k}\right|-\left|\Upsilon^{\pm}_{1k}-\Upsilon^{\pm}_{2k}+\Upsilon^{\pm}_{3k}\right|-\left|\Upsilon^{\pm}_{1k}-\Upsilon^{\pm}_{2k}-\Upsilon^{\pm}_{3k}\right|}{8\Upsilon^{\pm}_{1k}\Upsilon^{\pm}_{2k}},\tag{55}$$

completing the derivation of the SBP reconstruction.

3. RESULTS

3.A. Sine plate

3.A.1. Visualization of the reconstruction

Image acquisition is now simulated for a tomosynthesis system comparable to the Selenia Dimensions DBT unit (Hologic Inc., Bedford, MA) with an angular range (Θ) of 15°, assuming that the sine plate has a thickness (ε) of 0.10 mm and a frequency (f_0) of 2.0 lp/mm. Following our previous work,[3,4] the attenuation coefficient of the sine plate is normalized so that total attenuation is unity for the central projection for which $\theta = 0°$. Accordingly, we let $C = 1/(\varepsilon\sec\alpha_y)$. The denominator in this expression is the x-ray path length through the object for the central projection.

In Fig. 6, SBP reconstruction is displayed as a grayscale image in the xz plane, which is analogous to the plane of the chest wall in a breast application. The two subplots (a) and (b) correspond to two pitches for the sine plate; namely, 0° and 45°. An oscillatory pattern with the frequency of the input object is correctly resolved along both pitches. This finding illustrates that an input frequency with a pitch well outside the opening angle of the FDC can be resolved in tomosynthesis.

Figure 6 also shows that the reconstruction greatly overestimates the thickness of the sine plate due to backprojection artifacts. This result is observed at both the 0° and 45° pitches. Similar backprojection artifacts would not be present in a FBP reconstruction for CT with complete angular data ($\Theta = 180°$).

In a clinical application of DBT, the reconstruction is not typically viewed in the xz plane as it is shown in Fig. 6. Instead, the reconstruction is conventionally displayed as a series of slices oriented along a 0° pitch. In order to simulate the clinical display of a reconstruction more closely, signal should be plotted versus position (x) measured along a 0° pitch, regardless of the pitch of the input object. Figures 7(a)–7(c) show this result for a sine plate pitched at a 45° angle similar to Fig. 6(b). The three plots correspond to three different reconstruction depths (z) given by −3.0, 0, and +3.0 mm. By viewing these three slices, it is difficult to deduce that the input object is sinusoidal along a 45° pitch. Instead, the object appears as if it were a dampened sine wave whose maximum shifts along the x direction with increasing depth, z. The spacing between adjacent peaks near the maximum is approximately 0.34 mm, corresponding to a frequency of 2.9 lp/mm. This frequency does not match the input frequency (f_0) of 2.0 lp/mm. It should be noted that the sine plate actually spans a length of $\varepsilon\sec\alpha_y$, or 0.14 mm, within each slice in Figs. 7(a)–7(c). Signal extends across a much broader length than 0.14 mm due to backprojection artifacts, causing the dimension of the object within the slice to be greatly overestimated.

To demonstrate that the same object can be better visualized in an oblique reconstruction, the pitch of the slice is changed to 45° in Fig. 7(d). This slice is generated at the depth ($z'' = 0$) corresponding to the mid-thickness of the sine plate along the pitch axis. Figure 7(d) illustrates that signal is sinusoidal with the correct frequency, 2.0 lp/mm. For this reason, the 45° pitch is the preferred orientation for displaying slices for this object.

3.A.2. Modulation transfer function

To give further insight into Fig. 7(d), we now re-examine the formula for the reconstruction derived in Sec. 2, and show that signal in a slice along the pitch of the object is always sinusoidal with the correct frequency. According to Eqs. (35) and (39) giving the formula for the reconstruction, the signal is a linear combination of sinusoidal functions along the x'' direction. This result can be written in terms of one sinusoidal function using the trigonometric identity

$$A_1\cos(\beta)+A_2\sin(\beta)=\sqrt{A_1^2+A_2^2}\cos(\beta+\Phi),\tag{56}$$

where

$$\Phi = \arctan\left(\frac{A_2}{A_1}\right)+\begin{cases}-\pi/2, & A_1<0\\ +\pi/2, & A_2<0\end{cases}.\tag{57}$$

From Eqs. (35) and (39), it follows that

$$\mu_{\mathrm{FBP}} = \sqrt{A_1^2+A_2^2}\cos(2\pi x'' f_0+\Phi),\tag{58}$$

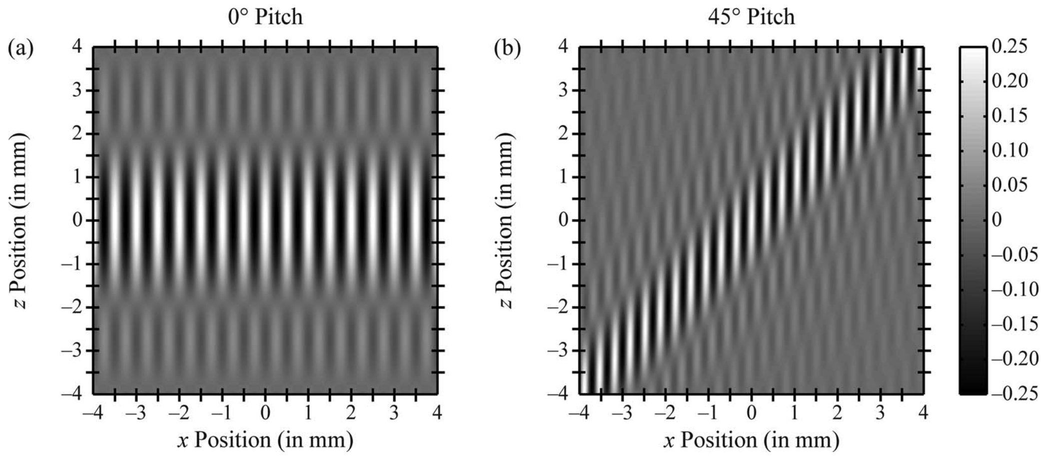

FIG. 6. The SBP reconstruction of a sine plate [Fig. 4(a)] is displayed as a grayscale image in the xz plane, assuming that $\Theta = 15^\circ$, $\varepsilon = 0.10$ mm, and $f_0 = 2.0$ lp/mm. While it is conventional to display the reconstruction with slices oriented along a 0° pitch (that is, with fixed values of z), this figure is useful for showing that an oscillatory pattern can be resolved along the two object pitches, 0° and 45°. The oscillatory pattern has the correct frequency along each pitch. Due to the limited angular range of the projections, backprojection artifacts cause the thickness of the object to be overestimated.

where

$$A_1 = C\varepsilon \begin{cases} \displaystyle\int_{\nu_-}^{\nu_+} \frac{\mathcal{F}_1\phi\left(\sqrt{f_0^2 + f_z''^2}\right)\cos(2\pi z'' f_z'')\mathrm{sinc}(\varepsilon f_z'')}{\sqrt{f_0^2 + f_z''^2}} df_z'', & 0 < \alpha_y \le 90^\circ - \Theta/2 \\ \displaystyle\int_{-\infty}^{\nu_+} \frac{\mathcal{F}_1\phi\left(\sqrt{f_0^2 + f_z''^2}\right)\cos(2\pi z'' f_z'')\mathrm{sinc}(\varepsilon f_z'')}{\sqrt{f_0^2 + f_z''^2}} df_z'' + \int_{\nu_-}^{\infty} \frac{\mathcal{F}_1\phi\left(\sqrt{f_0^2 + f_z''^2}\right)\cos(2\pi z'' f_z'')\mathrm{sinc}(\varepsilon f_z'')}{\sqrt{f_0^2 + f_z''^2}} df_z'', & 90^\circ - \Theta/2 < \alpha_y \le 90^\circ, \end{cases} \tag{59}$$

$$A_2 = C\varepsilon \begin{cases} \displaystyle\int_{\nu_-}^{\nu_+} \frac{\mathcal{F}_1\phi\left(\sqrt{f_0^2 + f_z''^2}\right)\sin(2\pi z'' f_z'')\mathrm{sinc}(\varepsilon f_z'')}{\sqrt{f_0^2 + f_z''^2}} df_z'', & 0 < \alpha_y \le 90^\circ - \Theta/2 \\ \displaystyle\int_{-\infty}^{\nu_+} \frac{\mathcal{F}_1\phi\left(\sqrt{f_0^2 + f_z''^2}\right)\sin(2\pi z'' f_z'')\mathrm{sinc}(\varepsilon f_z'')}{\sqrt{f_0^2 + f_z''^2}} df_z'' + \int_{\nu_-}^{\infty} \frac{\mathcal{F}_1\phi\left(\sqrt{f_0^2 + f_z''^2}\right)\sin(2\pi z'' f_z'')\mathrm{sinc}(\varepsilon f_z'')}{\sqrt{f_0^2 + f_z''^2}} df_z'', & 90^\circ - \Theta/2 < \alpha_y \le 90^\circ. \end{cases} \tag{60}$$

Equation (58) provides the desired formula for signal in a slice with the same pitch as the object. This formula proves that the signal is sinusoidal with the correct frequency (f_0). This result holds whether the slice is inside or outside the object.

In the pitched slice described by Eq. (58), the signal has a phase shift Φ that does not necessarily match the phase of the input object at each reconstruction depth, z''. If one considers the special case in which the depth of the slice is aligned with the mid-thickness of the sine plate ($z'' = 0$), it can be shown that Φ vanishes. Hence the phase of the signal matches the object

$$\mu_{\mathrm{FBP}}|_{z''=0} = G(f_0) \cdot C\cos(2\pi x'' f_0), \tag{61}$$

where

$$G(f_0) = \begin{cases} \varepsilon \displaystyle\int_{f_0\tan(\alpha_y - \Theta/2)}^{f_0\tan(\alpha_y + \Theta/2)} \frac{\mathcal{F}_1\phi\left(\sqrt{f_0^2 + f_z''^2}\right)\mathrm{sinc}(\varepsilon f_z'')}{\sqrt{f_0^2 + f_z''^2}} df_z'', & 0 < \alpha_y \le 90^\circ - \Theta/2 \\ \varepsilon \left[\displaystyle\int_{-\infty}^{f_0\tan(\alpha_y + \Theta/2)} \frac{\mathcal{F}_1\phi\left(\sqrt{f_0^2 + f_z''^2}\right)\mathrm{sinc}(\varepsilon f_z'')}{\sqrt{f_0^2 + f_z''^2}} df_z'' + \int_{f_0\tan(\alpha_y - \Theta/2)}^{\infty} \frac{\mathcal{F}_1\phi\left(\sqrt{f_0^2 + f_z''^2}\right)\mathrm{sinc}(\varepsilon f_z'')}{\sqrt{f_0^2 + f_z''^2}} df_z''\right], & 90^\circ - \Theta/2 < \alpha_y \le 90^\circ. \end{cases} \tag{62}$$

Equation (61) demonstrates that signal in the slice along the mid-thickness of the object is proportional to the attenuation coefficient of the sine plate. The proportionality factor, $G(f_0)$, is by definition the optical transfer function (OTF). The OTF compares the amplitude of signal in the image against the attenuation coefficient of the test object

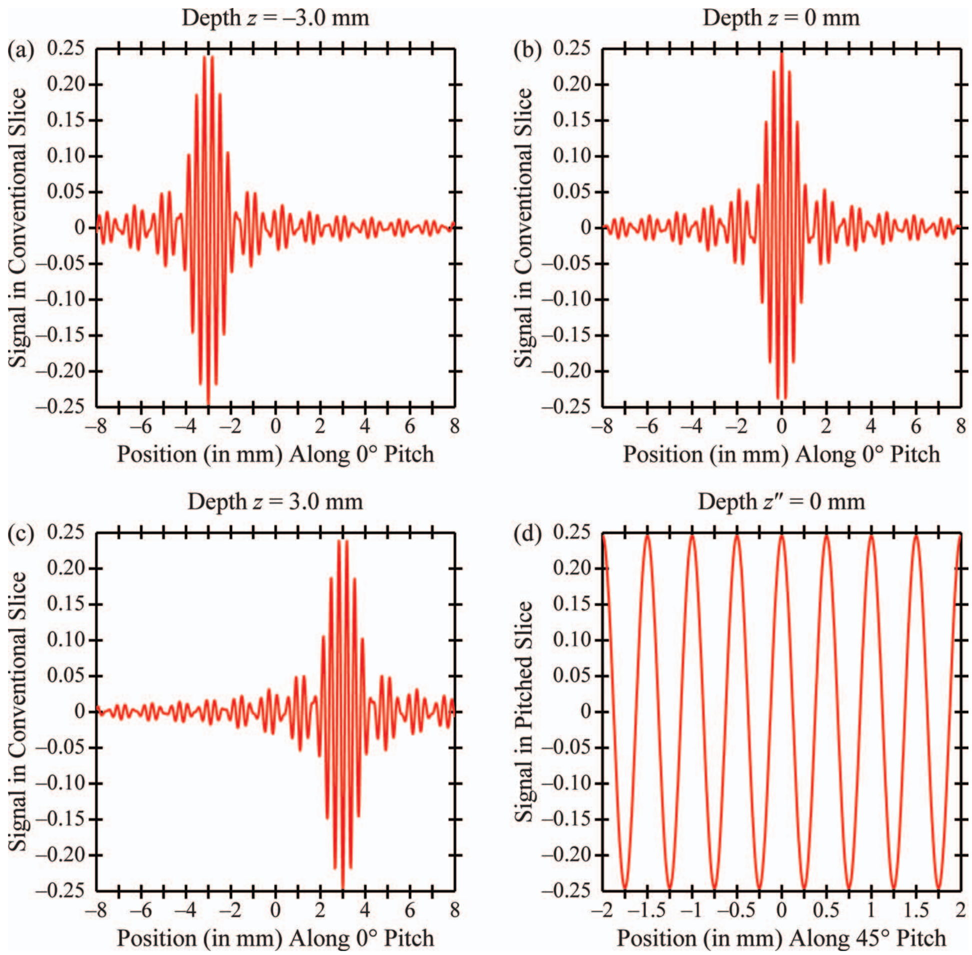

FIG. 7. (a)–(c) Following convention, the reconstruction in Fig. 6(b) is displayed using slices oriented along a 0° pitch. Each slice corresponds to a fixed depth z. It is difficult to deduce that the test object is sinusoidal along a 45° pitch. (d) In viewing a slice through the mid-thickness of the object at a 45° pitch ($z'' = 0$), it becomes clear that the attenuation coefficient is sinusoidal along this direction. For this reason, the 45° pitch is the preferred orientation for displaying slices through this object.

at all frequencies, f_0. Depending on the sign of the OTF, the phase shift relative to the input object is either 0° or 180°.

To investigate how image quality varies with pitch in an oblique reconstruction, the MTF is now derived from the OTF. The MTF is calculated by normalizing the modulus of $G(f_0)$ to the corresponding limit for which $f_0 \to 0$.[17] Appendix C shows that this limit can be evaluated in closed form for Case 1 of Sec. 2. To demonstrate that modulation is preserved, the MTF should approach unity:

$$\mathrm{MTF}(f_0) = \frac{|G(f_0)|}{\lim\limits_{f_0 \to 0} G(f_0)}. \quad (63)$$

In Fig. 8, the MTF is plotted versus frequency (f_0) and pitch (α_y) for four thicknesses of the sine plate: $\varepsilon = 0.01$, 0.10, 1.0, and 10.0 mm. The reconstruction technique is SBP. As expected, Fig. 8 demonstrates that the MTF decreases with frequency. This dependency is not quite monotonic at high frequencies exceeding the first zero of the MTF.

Figure 8 illustrates that the MTF is highly dependent upon the thickness of the object. If the object is very thin [Fig. 8(a)], the MTF is close to unity over a broad range of pitches and frequencies. As the object thickness is increased, the MTF decreases. This degradation in MTF is pronounced with increasing pitch and frequency. In accord with the predictions of the analytical model, experimental reconstructions of bar patterns also demonstrate that high frequency information is lost with increasing pitch (Fig. 3).

It is useful to explain the thickness dependency of the MTF in terms of Fourier theory. Recall that the Fourier transform of a sine plate consists of two lines modulated by a "sinc" function along the direction perpendicular to the pitch axis. Within the sampling cones of Fourier space, it can be shown that the amplitude of the "sinc" function increases as the object thickness is reduced (Fig. 2). This observation explains why the MTF of a thin object is larger than a thick object in Fig. 8.

At various object thicknesses, Fig. 8 provides a platform for calculating the highest frequency with detectable modulation in an oblique reconstruction. In Paper II of this series of papers, the highest detectable frequency is explicitly calculated under a more general set of modeling assumptions which include a pixelated detector and a 3D acquisition geometry.

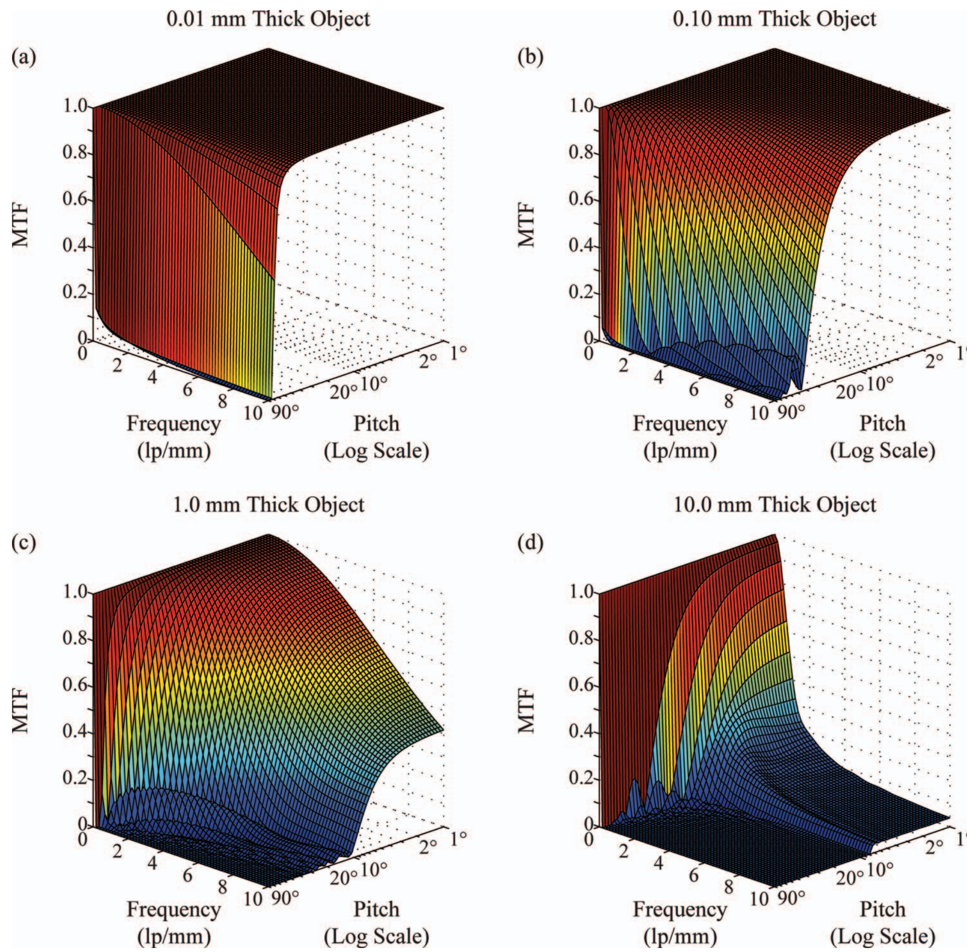

FIG. 8. The dependency of the in-plane MTF on frequency (f_0) and pitch (α_y) is analyzed using surface plots at four object thicknesses ($\varepsilon = 0.01$, 0.10, 1.0, and 10.0 mm). It is demonstrated that modulation is preserved over a broad range of pitches and frequencies if the object is thin. As the object thickness is increased, modulation is degraded. This loss of modulation is pronounced with increasing pitch and frequency. This finding is concordant with experimental images of bar patterns presented earlier in this work (Fig. 3), which also show that high frequency information is lost with increasing pitch.

3.B. Rod

With a similar acquisition geometry, SBP reconstructions of a rod at 0° and 45° pitches are now simulated (Fig. 9), assuming a rod length (Π) of 10.0 mm and a thickness (ε) of 0.10 mm. Grayscale images are displayed in the xz plane analogous to Fig. 6 showing the reconstruction of a sine plate. Due to backprojection artifacts, it is difficult to deduce that the input object is rectangular. However, it can be shown that the rod length is accurately determined from signal along the lines $z = 0$ and $z = x$ for the 0° and 45° pitches, respectively.

In conventional practice, the reconstruction is not displayed as a grayscale image in the xz plane, but instead, as a series of slices with a 0° pitch. To simulate this convention, signal is plotted versus x in Figs. 10(a)–10(c), assuming that the rod is pitched at a 45° angle. The three plots correspond to three depths within the rod; namely, $z = -3.0$, 0, and $+3.0$ mm. In a perfect reconstruction, each slice should be a rectangle function with length $\varepsilon \sec \alpha_y$, or 0.14 mm. Due to backprojection artifacts, the reconstruction actually appears trapezoidal, and the extent of the rod within each slice is greatly overestimated. At all three depths, the plateau length of the trapezoid is 6.0 mm and the full width at half maximum (FWHM) is 7.0 mm. Consequently, the conventional display of slices is not useful for this object.

The reconstruction more clearly resembles the input object if slices are generated along a 45° pitch, as shown in Fig. 10(d). In this plot, we simulate a slice at the depth $z'' = 0$, corresponding to the mid-thickness of the rod. As expected, signal is a rectangle function with a plateau length of 10.0 mm. This length matches known ground truth for the rod.

Figure 10(d) also investigates how the estimate of rod length is influenced by rod thickness. As the thickness is increased, it is demonstrated that signal appears more trapezoidal than rectangular, and thus the edge of the rod is blurred. To estimate rod length, one can calculate the FWHM of the trapezoid. With rod thicknesses of 0.1, 3.4, and 6.7 mm, the FWHM is exactly 10.0 mm in agreement with the actual rod length. By contrast, with a rod thickness of 10.0 mm, the FWHM is 10.6 mm. Consequently, the rod length at a 45° pitch is slightly overestimated if its thickness is comparable to its length.

To investigate how the measurement of the size of an object varies along different directions in the reconstruction, the

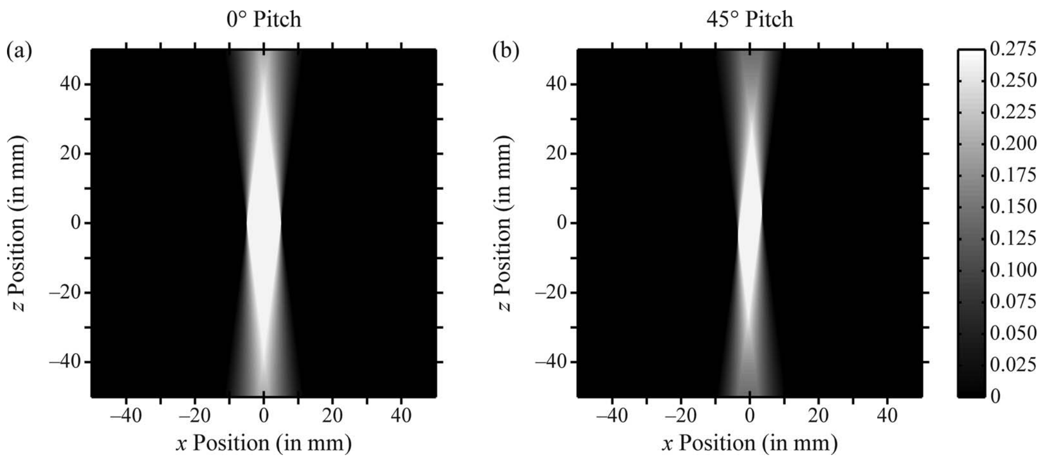

FIG. 9. The SBP reconstruction of a rod [Fig. 4(b)] is displayed as a grayscale image in the xz plane, assuming that $\Theta = 15°$, $\varepsilon = 0.10$ mm, and $\Pi = 10.0$ mm. One can show that the rod length of 10.0 mm is correctly determined along the two object pitches, 0° and 45°, by measuring signal along the lines $z = 0$ and $z = x$, respectively. Because projections are acquired over a limited angular range, there are backprojection artifacts that cause the thickness of the rod to be overestimated. In addition, the object does not appear to be rectangular in the reconstruction.

estimate of rod length is plotted versus pitch in Fig. 11(a). We continue to use the FWHM as the metric for estimating rod length in a pitched slice. Figure 11(a) shows that the estimate of rod length is accurate (10.0 mm) over a broad range of pitches if the object is thin. Increasing the rod thickness causes the length estimate to be accurate over a narrower range of pitches; all inaccuracies are overestimates of rod length.

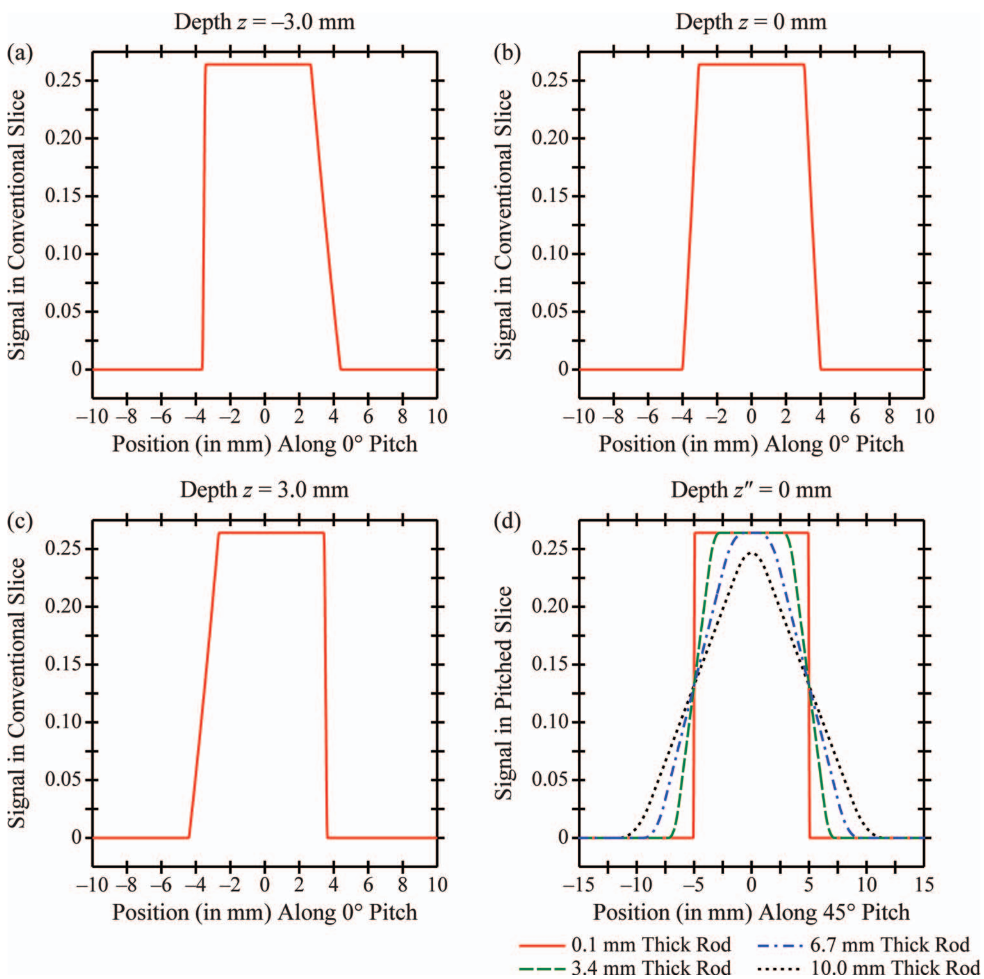

FIG. 10. (a)–(c) By displaying the reconstruction in Fig. 9(b) with conventional slices oriented along a 0° pitch, it is difficult to deduce the length of a rod whose long axis is oblique (45° pitch). Due to backprojection artifacts, signal spans a much greater length than expected; signal in each slice should be a rectangle function with length 0.14 mm. (d) The rod length can be correctly determined if slices are generated through the mid-thickness of the object at a 45° pitch ($z'' = 0$). Increasing the thickness of the object causes the edges of the rod to be blurred.

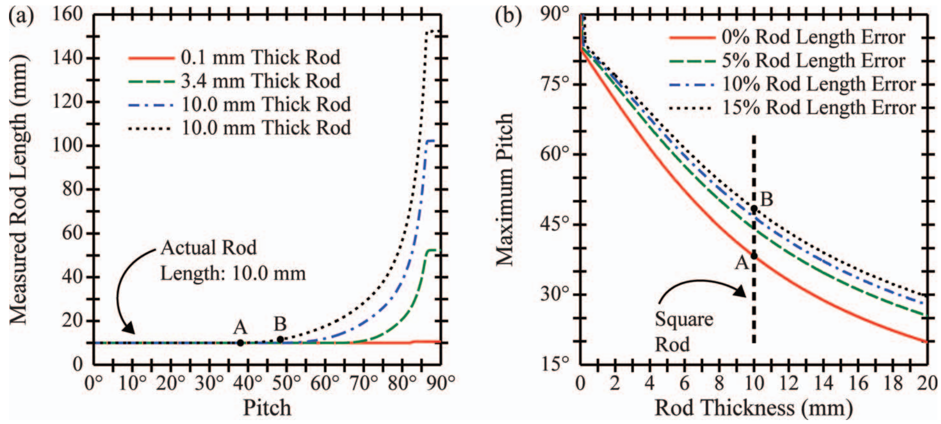

FIG. 11. (a) The length of a rod is determined at various pitches using oblique reconstructions. The FWHM of signal in pitched slices [Fig. 10(d)] is the metric used to estimate rod length; the actual length is 10.0 mm. (b) At various rod thicknesses, one can use Fig. 11(a) to determine the maximum pitch at which rod length can be correctly measured. This maximum pitch is plotted versus rod thickness for different levels of error tolerance in the measurement of rod length. It is demonstrated here that rod length is correctly determined over a broad range of pitches if the object is thin, but over a narrower range of pitches if the object is thick.

Figure 11(b) illustrates the thickness dependency of the maximum pitch at which rod length can be correctly determined. As shown, the maximum pitch decreases with rod thickness. In the special case of an extremely thin rod, the rod length can be correctly determined up to a 90° pitch.

The consequences of permitting error in the estimate of rod length are also explored in Fig. 11. It is shown that the introduction of error tolerance broadens the range of pitches at which the estimate of rod length is acceptable. For example, if the rod is square, the length estimate is exact up to a pitch of 38°, but is acceptable up to a pitch of 48° with an error tolerance of 15% (Points A and B, respectively, in Fig. 11).

4. COMPARISON WITH RESULTS IN THE LITERATURE

In this paper, the MTF is calculated by comparing the amplitude of the image against the attenuation coefficient of a sinusoidal test object at various frequencies. Previous authors such as Zhao[2] have proposed a different formulation for MTF in tomosynthesis. Zhao's work draws a distinction between in-plane MTF and 3D MTF. In Zhao's formulation, the in-plane MTF is the integral of the 3D MTF along the z direction. This approach presumes that the z direction is perpendicular to the slice.[2] To generalize Zhao's calculation of in-plane MTF to oblique planes, we now show that the line integral should be performed along a more general direction perpendicular to the slice. To this end, one must first deduce the OTF of the entire reconstruction space using the expression for in-plane OTF derived in Eq. (62):

$$H(f_x, f_z) = \frac{\mathcal{F}_1\phi\left(\sqrt{f_x^2 + f_z^2}\right)}{\sqrt{f_x^2 + f_z^2}} \cdot \operatorname{rect}\left(\frac{f_z}{2f_x \tan(\Theta/2)}\right). \tag{64}$$

In Eq. (64), the rect function models the FDC whose opening angle matches the angular range of the scan [Fig. 1(b)]. Although Eq. (64) is derived from Eq. (62), it can be shown that Eq. (64) is equivalent to the Fourier transform of the point spread function (PSF). This result follows directly from Eq. (14) noting that the Fourier transform of a point-like input object is unity; that is, $\mathcal{F}_2\mu(f_r \cos\zeta, f_r \sin\zeta) = 1$. The formula below demonstrates that the in-plane OTF [Eq. (62)] can be expressed as a line integral of the OTF of the entire reconstruction space [Eq. (64)]:

$$G(f_0) = \int_{-\infty}^{\infty} H(f_x'', f_z'')\big|_{f_x''=f_0}\, \varepsilon \cdot \operatorname{sinc}(\varepsilon f_z'')df_z'', \tag{65}$$

where

$$H(f_x'', f_z'') = \frac{\mathcal{F}_1\phi\left(\sqrt{f_x''^2 + f_z''^2}\right)}{\sqrt{f_x''^2 + f_z''^2}} \cdot \operatorname{rect}\left(\frac{f_x'' \sin\alpha_y + f_z'' \cos\alpha_y}{2\left[f_x'' \cos\alpha_y - f_z'' \sin\alpha_y\right]\tan(\Theta/2)}\right). \tag{66}$$

Since the line integral in Eq. (65) is performed along a general direction (f_z'') which is perpendicular to the pitch of the slice, this result generalizes Zhao's formulation of in-plane OTF to oblique planes.

Although Zhao does not model the thickness of an object in the reconstruction, this paper demonstrates that the in-plane MTF is indeed dependent upon the object thickness (Fig. 8). This property arises from the term $\varepsilon \cdot \operatorname{sinc}(\varepsilon f_z'')$ in the in-plane MTF calculation [Eq. (65)]. Recall that this term is the Fourier transform of the function $\operatorname{rect}(z''/\varepsilon)$, which models the object thickness ε along the direction perpendicular to the slice [Eq. (17)]. In summary, this paper introduces the object thickness as an additional parameter for quantification of in-plane MTF, thus generalizing Zhao's model of image quality.

5. DISCUSSION

By convention, a tomosynthesis reconstruction is created with slices parallel to the detector. This work demonstrates from first principles that oblique slices are also justified. To assess how individual frequencies in the MTF are preserved in oblique reconstructions, a sine plate is simulated along various pitches. Although this object is not properly visualized in conventional slices generated along a 0° pitch, the sinusoidal attenuation coefficient is perfectly resolved in slices created along the pitch of the test frequency.

To analyze whether the length of an object can be correctly determined along various pitches, the reconstruction of a rod is also simulated. It is shown that backprojection artifacts in conventional slices oriented along a 0° pitch cause the extent of the object to be greatly overestimated with SBP reconstruction. By contrast, backprojection artifacts are minimal in a pitched slice oriented along the length of the rod.

In linear systems theory, the MTF of a single projection image is calculated without making reference to the thickness of the test frequency.[17] This work demonstrates that the in-plane MTF of a tomosynthesis reconstruction is indeed dependent upon the object thickness. Previous authors such as Zhao have not introduced the object thickness as a parameter in the MTF calculation.[2]

According to this work, a very thin object can be reconstructed at large pitches approaching 90°. This property does not hold as the thickness of the object is increased; in particular, it is shown that the MTF is degraded and that the measurement of rod length is inaccurate at large pitches. Because a clinical image consists of objects with a range of thicknesses, a clinical reconstruction is not expected to be valid up to pitches approaching 90°. Future work is merited to determine the range of pitches at which clinical reconstructions are appropriate in tomosynthesis; however, anecdotal results suggest that pitches approaching 45° are viable.

In CT, reconstructions can be generated along any planar or curved surface in the imaging volume using MPR.[1] Although this work on oblique reconstructions is implicitly limited to planar slices, it is reasonable to posit that tomosynthesis reconstructions are also justifiable with curved surfaces. Displaying a blood vessel or a vascular calcification cluster in a single view is a potential application for curved planar reformatting in DBT. It is conceivable that the full extent of these tortuous structures cannot be visualized using conventional slices oriented along a 0° pitch. Justifying the feasibility of MPR along any curved surface would be difficult with analytical modeling. For this reason, future studies should investigate these reconstructions in computer anthropomorphic phantoms and in clinical cases.

This study could also be expanded by considering multiple test objects in the reconstruction. Although this work calculates the backprojection artifacts of a single test object, it does not investigate whether the backprojection artifacts of one object could hide another object. For example, it would be useful to investigate whether the backprojection artifacts of a mass impact the modulation of a sine plate or the length estimate of a rod (e.g., a spiculation).

This work shows that a pitched slice is the preferred orientation for viewing some test objects in the reconstruction. In theoretical calculations, choosing the optimal pitch for viewing an object is trivial, since the actual pitch of the object is known. Choosing the optimal pitch will be more challenging in clinical cases in which there are out-of-focus artifacts and ground truth is lacking. The development of a framework for determining the optimal pitch for viewing a clinical reconstruction remains the subject of future work. Quantifying the precise size of an asymmetric mass prior to surgical resection is one application where matching the pitch of the reconstruction to the long axis of a lesion is potentially important.

While filtering is modeled in the FBP formulas of Sec. 2, the reconstructions that are plotted in Sec. 3 do not apply filtering (Figs. 6–11). Instead, the reconstructions use simple backprojection. Recalling Eq. (61), it can be shown that filtering is not critical in displaying a slice through the mid-thickness of a pitched sine plate [Fig. 9(d)]. According to this expression, signal is sinusoidal with the correct frequency, regardless of filter. Consequently, introducing a filter would not change the relative signal in the pitched slice in Fig. 7(d).

Although the ramp filter is the basis for image reconstruction in CT,[2,15,18] we now explain why this work suggests that the ramp filter is not optimal for tomosynthesis. In the OTF identity that is derived in Appendix C [Eq. (C6)], it is important to note that $G(0)$ is proportional to $\mathcal{F}_1\phi(0)$, or the filter evaluated at zero frequency. In normalizing $G(f_0)$ by $G(0)$ to calculate the in-plane MTF [Eq. (63)], it follows from Appendix C that the quotient is infinite if $\mathcal{F}_1\phi(0) = 0$. Hence, the in-plane MTF is not well-defined if ramp filtering is used. Our previous work on super-resolution in DBT also concluded that the ramp filter is not optimal, since modulation is zero in the reconstruction of a test frequency perpendicular to the plane of x-ray tube motion.[4] Future work on filter optimization is merited for these reasons. Although this work calculates the in-plane MTF for SBP reconstruction only, it is expected that this result is dependent on the filter [Eq. (62)].

Some of the limitations of this work and directions for future analytical modeling are now noted. Although a 2D simulation with a parallel-beam geometry was sufficient for a proof-of-principle justification for oblique reconstructions, it will be important to extend this work to a 3D simulation with a divergent-beam geometry. In addition, future studies should model the presence of discrete step angles between projections as well as a more general detector that rotates between projections. Finally, the presence of a thin-film transistor array,[19–21] which samples digital detector signal in pixels, should also be simulated.[22–24]

6. CONCLUSION

Conventional practice is to generate a tomosynthesis reconstruction using slices parallel to the detector. This work demonstrates that slices can also be generated along oblique directions through the same volume. It is shown that the object must be thin in order to be displayed with high image quality in an oblique reconstruction. In the ACR Mammography Accreditation Phantom, this thickness constraint is satisfied by the three test objects (spheres, rods, and specks), which have been designed to simulate clinically important structures.

It should be emphasized that the results presented in this study are valid in any application of tomosynthesis, not simply breast applications. In addition, although the beam in each projection is presumed to consist of x rays, the calculations in this work are applicable to electromagnetic radiation at any energy, as well as to beams consisting of particles (e.g., neutron tomosynthesis).

ACKNOWLEDGMENTS

The authors thank David Pokrajac (Delaware State University, Dover, DE) for giving comments on early drafts of the derivation of the reconstruction of a rod. In addition, the authors thank Roshan Karunamuni (University of Pennsylvania, Philadelphia, PA) for helping with the assembly of the goniometry stand used for orienting the bar pattern phantom along various pitches for experimental images (Fig. 3). Finally, we acknowledge Johnny Kuo, Susan Ng, and Peter Ringer (Real Time Tomography, LLC, Villanova, PA) for providing technical assistance relating to the Briona™ software used to create reconstructions of the bar pattern phantom. Andrew D. A. Maidment is a member of the Scientific Advisory Board of Real Time Tomography. The project described was supported by predoctoral training Grant No. W81XWH-11-1-0100 through the Department of Defense Breast Cancer Research Program. The content is solely the responsibility of the authors and does not necessarily represent the official views of the funding agency. Support for Real Time Tomography was provided separately in part through NIH Grant No. R43EB007140/R44EB007140.

APPENDIX A: RADON TRANSFORM OF PITCHED SINE PLATE

In Fig. 4, plots of the Radon transform are shown versus t at a fixed projection angle (θ) for the two test objects. In order to derive the plot for the sine plate [Fig. 4(a)], we now calculate the Radon transform from first principles. Recall that the 2D Fourier transform of this object is

$$\begin{aligned}\mathcal{F}_2\mu(f_x, f_z) = \frac{C\varepsilon}{2}[&\delta(f_x\cos\alpha_y + f_z\sin\alpha_y - f_0)\\ &+ \delta(f_x\cos\alpha_y + f_z\sin\alpha_y + f_0)]\\ &\cdot \mathrm{sinc}[\varepsilon(-f_x\sin\alpha_y + f_z\cos\alpha_y)]. \qquad \text{(A1)}\end{aligned}$$

This result follows from Eq. (22) using the transformation between the (f_x'', f_z'') and (f_x, f_z) coordinate systems [Eq. (21)]. According to the Central Slice Theorem [Eq. (3)], this 2D Fourier transform can be related to the Radon transform as follows:

$$\mathcal{R}\mu(t,\theta) = \int_{-\infty}^{\infty} \mathcal{F}_2\mu(f_r\cos\theta, f_r\sin\theta)\cdot e^{2\pi i f_r t}df_r \qquad \text{(A2)}$$

$$\begin{aligned}&= \int_{-\infty}^{\infty} \frac{C\varepsilon}{2}(\delta[f_r\cos(\theta-\alpha_y) - f_0]\\ &+ \delta[f_r\cos(\theta-\alpha_y) + f_0])\\ &\cdot \mathrm{sinc}[\varepsilon f_r\sin(\theta-\alpha_y)]\cdot e^{2\pi i f_r t}df_r. \qquad \text{(A3)}\end{aligned}$$

In order to simplify Eq. (A3), one must assume that $\theta \neq 90^\circ + \alpha_y$, so that the two delta functions can be evaluated with the identity

$$\begin{aligned}\delta[f_r\cos(\theta-\alpha_y) \pm f_0] &= \delta[f_r \pm f_0\sec(\theta-\alpha_y)]\\ &\cdot \sec(\theta-\alpha_y). \qquad \text{(A4)}\end{aligned}$$

Due to an infinity in the secant function, Eq. (A4) is undefined if $\theta = 90^\circ + \alpha_y$. This constraint corresponds to the projection for which each ray is parallel with the long axis of the sine plate. The Radon transform cannot be written in closed form for this projection, since the total x-ray attenuation is undefined along an infinite path length:

$$\mathcal{R}\mu(t, 90^\circ + \alpha_y) = \begin{cases}\text{undefined}, & -\varepsilon/2 \le t \le \varepsilon/2\\ 0, & \text{otherwise}\end{cases}. \qquad \text{(A5)}$$

Although the Radon transform cannot be written in closed form if $\theta = 90^\circ + \alpha_y$, it can indeed be written in closed form for the projection angle illustrated in Fig. 4(a). Combining Eqs. (A3) and (A4) yields

$$\begin{aligned}\mathcal{R}\mu(t,\theta) &= \frac{C\varepsilon}{2}\cdot\sec(\theta-\alpha_y)\mathrm{sinc}[\varepsilon f_0\tan(\theta-\alpha_y)]\\ &\cdot\left(e^{2\pi i f_0 t\sec(\theta-\alpha_y)} + e^{-2\pi i f_0 t\sec(\theta-\alpha_y)}\right) \qquad \text{(A6)}\end{aligned}$$

$$\begin{aligned}&= C\varepsilon\sec(\theta-\alpha_y)\mathrm{sinc}[\varepsilon f_0\tan(\theta-\alpha_y)]\\ &\cdot\cos[2\pi f_0 t\sec(\theta-\alpha_y)]. \qquad \text{(A7)}\end{aligned}$$

This result proves that the Radon transform has sinusoidal dependence on t, as indicated in the figure. Consistent with Eq. (A7), the plot has no phase shift relative to the origin, $t = 0$.

APPENDIX B: RADON TRANSFORM OF PITCHED ROD

In Fig. 4(b), the Radon transform of a pitched rod is plotted versus t at a fixed projection angle (θ). To derive this plot, we now calculate the Radon transform from first principles. Using Eqs. (21) and (41), it can be shown that the 2D Fourier transform of this object is

$$\begin{aligned}\mathcal{F}_2\mu(f_x, f_z) &= C\Pi\varepsilon\cdot\mathrm{sinc}[\Pi(f_x\cos\alpha_y + f_z\sin\alpha_y)]\\ &\cdot\mathrm{sinc}[\varepsilon(-f_x\sin\alpha_y + f_z\cos\alpha_y)]. \qquad \text{(B1)}\end{aligned}$$

From Eq. (A2), it follows that

$$\begin{aligned}\mathcal{R}\mu(t,\theta) &= C\Pi\varepsilon\int_{-\infty}^{\infty}\mathrm{sinc}[\Pi f_r\cos(\theta-\alpha_y)]\\ &\cdot\mathrm{sinc}[\varepsilon f_r\sin(\theta-\alpha_y)]\cdot e^{2\pi i f_r t}df_r. \qquad \text{(B2)}\end{aligned}$$

Similar to Appendix A, one must consider two separate constraints in order to evaluate the Radon transform; namely, $\theta = 90^\circ + \alpha_y$ and $\theta \neq 90^\circ + \alpha_y$. If one first considers the constraint $\theta = 90^\circ + \alpha_y$, the integral in Eq. (B2) simplifies to

$$\mathcal{R}\mu(t, 90^\circ+\alpha_y) = C\Pi\varepsilon\int_{-\infty}^{\infty}\mathrm{sinc}(\varepsilon f_r)\cdot e^{2\pi i f_r t}df_r \qquad \text{(B3)}$$

$$= C\Pi\cdot\mathrm{rect}\left(\frac{t}{\varepsilon}\right). \qquad \text{(B4)}$$

This result corresponds to the projection for which each ray is parallel to the pitch axis (x''). The Radon transform is a rectangular function of t; the width of this function matches the rod thickness (ε). If one next considers the constraint $\theta \neq 90^\circ + \alpha_y$, the convolution theorem can be used to simplify Eq. (B2):

$$\begin{aligned}\mathcal{R}\mu(t,\theta \neq 90^\circ + \alpha_y)\\ &= C\Pi\varepsilon \cdot \mathcal{F}_1^{-1}\mathrm{sinc}[\Pi f_r \cos(\theta-\alpha_y)]\\ &\quad *_1 \mathcal{F}_1^{-1}\mathrm{sinc}[\varepsilon f_r \sin(\theta-\alpha_y)], \end{aligned} \tag{B5}$$

$$\begin{aligned} &= C\Pi\varepsilon \cdot \frac{1}{\Pi\cos(\theta-\alpha_y)}\mathrm{rect}\left[\frac{t}{\Pi\cos(\theta-\alpha_y)}\right]\\ &\quad *_1 \frac{1}{\varepsilon\sin(\theta-\alpha_y)}\mathrm{rect}\left[\frac{t}{\varepsilon\sin(\theta-\alpha_y)}\right].\end{aligned} \tag{B6}$$

In order to analyze the dependency of the Radon transform on t, it is useful to review the equation of an isosceles trapezoid

$$\begin{aligned}\mathcal{R}\mu(t,\theta \neq 90^\circ + \alpha_y)\\ &= B\cdot \mathrm{rect}\left[\frac{t}{(q_1+q_2)/2}\right]\\ &\quad *_1 \frac{1}{(q_2-q_1)/2}\mathrm{rect}\left[\frac{t}{(q_2-q_1)/2}\right]\end{aligned} \tag{B7}$$

$$= B\cdot \begin{cases} 1, & |t| \le \dfrac{q_1}{2}\\ \dfrac{-1}{(q_2-q_1)/2}\left(|t| - \dfrac{q_2}{2}\right), & \dfrac{q_1}{2} < |t| \le \dfrac{q_2}{2}\\ 0, & |t| > \dfrac{q_2}{2}\end{cases}, \tag{B8}$$

where B is the height of the plateau, q_1 is the length of the plateau, and q_2 is the length of the base. The trapezoid is symmetric about the origin, $t = 0$. Assuming that $-90^\circ < \theta \le 90^\circ$ and that $0 \le \alpha_y \le 90^\circ$, as stipulated in the body of this work, Eqs. (B6) and (B7) can be equated to yield

$$B = \begin{cases} C\varepsilon\sec(\theta-\alpha_y), & \theta < \alpha_y + \arctan\left(\dfrac{\Pi}{\varepsilon}\right)\\ C\Pi\csc(\theta-\alpha_y), & \theta > \alpha_y + \arctan\left(\dfrac{\Pi}{\varepsilon}\right)\end{cases}, \tag{B9}$$

$$q_1 = \begin{cases} \Pi\cos(\theta-\alpha_y) - \varepsilon\sin(\theta-\alpha_y), & \theta < \alpha_y + \arctan\left(\dfrac{\Pi}{\varepsilon}\right)\\ \varepsilon\sin(\theta-\alpha_y) - \Pi\cos(\theta-\alpha_y), & \theta > \alpha_y + \arctan\left(\dfrac{\Pi}{\varepsilon}\right)\end{cases}, \tag{B10}$$

$$q_2 = \Pi\cos(\theta-\alpha_y) + \varepsilon\sin(\theta-\alpha_y). \tag{B11}$$

This result provides a justification for the trapezoidal plot in Fig. 4(b) showing the Radon transform of the rod at a fixed projection angle (θ).

Although not plotted in Fig. 4(b), two degenerate cases in the formula for the trapezoid [Eq. (B7)] are noted for completeness. One degeneracy occurs if the plateau and base of the trapezoid have the same length ($q_1 = q_2$). Using Eqs. (B10) and (B11), it can be shown that this property occurs if $\theta = \alpha_y$:

$$\mathcal{R}\mu(t,\alpha_y) = C\varepsilon\cdot\mathrm{rect}\left(\frac{t}{\Pi}\right). \tag{B12}$$

This degeneracy corresponds to the projection in which the rays are perpendicular to the pitch axis. It is also useful to examine a second degenerate case in which the length of the plateau of the trapezoid is zero ($q_1 = 0$), while the length of the base is nonzero ($q_2 > 0$). This degeneracy occurs if the lengths of the two rectangle functions in Eq. (B6) are equivalent.

$$\begin{aligned}\mathcal{R}\mu\left(t,\alpha_y + \arctan\left(\frac{\Pi}{\varepsilon}\right)\right)\\ &= C\sqrt{\varepsilon^2+\Pi^2}\cdot\begin{cases} 1 - \dfrac{|t|\sqrt{\varepsilon^2+\Pi^2}}{\Pi\varepsilon}, & |t| \le \dfrac{\Pi\varepsilon}{\sqrt{\varepsilon^2+\Pi^2}}\\ 0, & |t| > \dfrac{\Pi\varepsilon}{\sqrt{\varepsilon^2+\Pi^2}}\end{cases}.\end{aligned} \tag{B13}$$

The Radon transform is no longer a trapezoidal function of t but instead is a triangular function of t. Unlike the projection illustrated in Fig. 4(b), it can be shown that this degenerate case corresponds to the projection in which one of the rays intercepts two corners of the rod. In the projection shown in Fig. 4(b), a ray that intercepts one corner of the rod does not strike the other corner.

APPENDIX C: OPTICAL TRANSFER FUNCTION IDENTITY

In this study, the MTF of a pitched reconstruction slice is calculated by normalizing the OTF to its value in the limit $f_0 \to 0$ [Eq. (63)]. It is difficult to evaluate this limit in closed form using Eq. (62), since the integration limits both tend toward zero. For this reason, we now provide a more direct method for evaluating $G(0)$ by explicitly calculating the reconstruction of a sine plate with zero frequency. This object is an infinitely long rod whose long axis is oriented along the pitch α_y and whose thickness is ε.

It is first necessary to evaluate the Radon transform of the object by substituting $f_0 = 0$ into Eq. (A7):

$$\mathcal{R}\mu(t,\theta) = C\varepsilon \sec(\theta - \alpha_y). \tag{C1}$$

As discussed in Appendix A, this result presumes that $\theta \neq 90^\circ + \alpha_y$. Recalling Sec. 2, it can be shown that this inequality holds at all projections angles for Case 1 of the reconstruction (Sec. 2.B.1). Hence

$$\mu_{\mathrm{FBP}}(x,z) = \int_{-\Theta/2}^{\Theta/2}\int_{-\infty}^{\infty}\phi(\tau) \cdot \mathcal{R}\mu(x\cos\theta + z\sin\theta - \tau, \theta)\,d\tau\,d\theta \tag{C2}$$

$$= \left[\int_{-\infty}^{\infty}\phi(\tau)d\tau\right]\left[\int_{-\Theta/2}^{\Theta/2}\mathcal{R}\mu \cdot d\theta\right]. \tag{C3}$$

The transition from Eq. (C2) to Eq. (C3) is justified because the Radon transform in Eq. (C1) is independent of t. The first term in Eq. (C3) is the integral of the filter ϕ over all space. From Fourier theory, this integral is equivalent to $\mathcal{F}_1\phi(0)$. The second term in Eq. (C3) is

$$\int_{-\Theta/2}^{\Theta/2}\mathcal{R}\mu \cdot d\theta = \int_{-\Theta/2}^{\Theta/2} C\varepsilon \sec(\theta - \alpha_y)d\theta, \tag{C4}$$

$$= C\varepsilon \ln\left|\frac{\sec(\alpha_y - \Theta/2) - \tan(\alpha_y - \Theta/2)}{\sec(\alpha_y + \Theta/2) - \tan(\alpha_y + \Theta/2)}\right|. \tag{C5}$$

Combining Eqs. (C3) and (C5) yields

$$G(0) = \mathcal{F}_1\phi(0) \cdot \varepsilon \ln\left|\frac{\sec(\alpha_y - \Theta/2) - \tan(\alpha_y - \Theta/2)}{\sec(\alpha_y + \Theta/2) - \tan(\alpha_y + \Theta/2)}\right|, \tag{C6}$$

completing the derivation of the OTF identity. If one considers the special case of SBP reconstruction, the substitution $\mathcal{F}_1\phi(f_r) = \mathcal{F}_1\phi(0) = 1$ should be made in Eq. (C6).

It would be difficult to perform an analogous derivation of $G(0)$ in considering Case 2 of Sec. 2, since the x-ray beam is aligned with the pitch axis of the rod in the projection for which $\theta = 90^\circ + \alpha_y$. At this projection angle, the Radon transform cannot be written in closed form:

$$\mathcal{R}\mu(t, 90^\circ + \alpha_y) = \begin{cases} \infty, & -\varepsilon/2 \le t \le \varepsilon/2 \\ 0, & \text{otherwise} \end{cases}. \tag{C7}$$

Because it would be difficult to evaluate a reconstruction using a Radon transform with an infinity, we evaluate $G(0)$ numerically in considering Case 2. This result can be derived from the integral in Eq. (62) in the limit $f_0 \to 0$.

APPENDIX D: NOMENCLATURE

Symbol	Meaning
$*$	Convolution operator (subscript denotes dimension)
$\in$	Set membership
$\mathcal{B}$	Backprojection operator
$\mathcal{F}$	Fourier transform operator (subscript denotes dimension)
$\mathcal{L}(t,\theta)$	Line that intercepts the point $(t\cos\theta,\ t\sin\theta)$ and that is perpendicular to the unit vector $\mathbf{p} = (\cos\theta)\mathbf{i} + (\sin\theta)\mathbf{k}$
$\mathcal{R}$	Radon transform operator
$\mathbb{R}^2$	Euclidean 2-space
$\mathbb{Z}$	Set of integers
α_y	Pitch angle, corresponding to a rotation about the y axis
β	Real number used to illustrate an identity involving the linear combination of a sine and a cosine function [Eq. (56)]
δ	Delta function
ε	Thickness of sine plate or rod (Fig. 4)
ζ	Polar angle of 2D frequency vector
θ	Projection angle (defined in Fig. 4).
Θ	Angular range of tomosynthesis scan
μ	X-ray linear attenuation coefficient of test object
$\nu_\pm$	A quantity defined by Eq. (31) to simplify intermediate calculations (Fig. 5)
Π	Rod length (Fig. 4).
$\Upsilon_{jk}^{\pm}$	Terms defined by Eqs. (46)–(48) used to simplify intermediate calculations, where j varies from 1 to 3
ϕ	Reconstruction filter
Φ	A quantity defined by Eq. (57) used to simplify intermediate calculations
A_1, A_2	Quantities defined by Eqs. (59) and (60) used to simplify intermediate calculations
ACR	American College of Radiology
B	Height of plateau of trapezoid used for calculating the Radon transform of a pitched rod [Eq. (B7)]
b_1,b_2	Real numbers used to illustrate an angle sum trigonometric identity [Eq. (34)]
BPF	Backprojection filtering
C	Maximum value of attenuation coefficient of sine plate or rod
CT	Computed tomography
DBT	Digital breast tomosynthesis
DM	Digital mammography
f	Spatial frequency (subscript denotes direction of measurement)
f_0	Input frequency of a sine plate
f''_{zj}	A quantity defined by Eq. (37) used to simplify intermediate calculations

f_{zk}	A quantity defined by Eq. (45) used to simplify intermediate calculations
FBP	Filtered backprojection
FDC	Fourier double cone (defined by Fig. 1)
FWHM	Full width at half maximum
$G(0)$	In-plane OTF evaluated at zero frequency
$G(f_0)$	In-plane OTF evaluated at the frequency f_0 [Eq. (62)]
$H(f_x, f_z)$	OTF of the reconstruction [Eq. (64)]
i	Imaginary unit given as $\sqrt{-1}$
$I^{\pm}_{k,\mathrm{SBP}}$	An integral defined by Eqs. (53) and (54)
lp	Line pairs
LS	Linear systems
MTF	Modulation transfer function
OTF	Optical transfer function
$\mathbf{p}$	Unit vector given by $(\cos\theta)\mathbf{i} + (\sin\theta)\mathbf{k}$ (Fig. 4)
PSF	Point spread function
q_1	Length of plateau of trapezoid used for calculating the Radon transform of a pitched rod [Eq. (B7)]
q_2	Length of base of trapezoid used for calculating the Radon transform of a pitched rod [Eq. (B7)]
s	Free parameter ranging between $-\infty$ and ∞ used in the parametric representation of the line $\mathcal{L}(t,\theta)$ [Eq. (1)]
SBP	Simple backprojection
t	Affine parameter of Radon transform [Eq. (1)]
(x, z)	Point in space

[a)]Author to whom correspondence should be addressed. Electronic mail: Andrew.Maidment@uphs.upenn.edu; Telephone: +1-215-746-8763; Fax: +1-215-746-8764.

[1]J. Hsieh, "Image presentation," *Computed Tomography: Principles, Design, Artifacts, and Recent Advances* (SPIE, Bellingham, WA, 2003), Chap. 4, pp. 99–111.

[2]B. Zhao and W. Zhao, "Three-dimensional linear system analysis for breast tomosynthesis," Med. Phys. **35**(12), 5219–5232 (2008).

[3]R. J. Acciavatti and A. D. A. Maidment, "Investigating the potential for super-resolution in digital breast tomosynthesis," Proc. SPIE **7961**, 79615K-1–79615K-12 (2011).

[4]R. J. Acciavatti and A. D. A. Maidment, "Observation of super-resolution in digital breast tomosynthesis," Med. Phys. **39**(12), 7518–7539 (2012).

[5]J. Kuo, P. A. Ringer, S. G. Fallows, P. R. Bakic, A. D. A. Maidment, and S. Ng, "Dynamic reconstruction and rendering of 3D tomosynthesis images," Proc. SPIE **7961**, 796116-1–796116-11 (2011).

[6]E. A. Rafferty, "Tomosynthesis: New weapon in breast cancer fight," Decisions in Imaging Economics **17**(4) (2004).

[7]S. P. Poplack, T. D. Tosteson, C. A. Kogel, and H. M. Nagy, "Digital breast tomosynthesis: Initial experience in 98 women with abnormal digital screening mammography," Am. J. Roentgenol. **189**(3), 616–623 (2007).

[8]J. M. Park, A. Edmund, J. Franken, M. Garg, L. L. Fajardo, and L. T. Niklason, "Breast tomosynthesis: Present considerations and future applications," Radiographics **27**, S231–S240 (2007).

[9]ACR, "Mammography quality control tests," *Mammography Quality Control Manual* (American College of Radiology, Reston, VA, 1999), pp. 231–294.

[10]J. Hsieh, "Image reconstruction," *Computed Tomography: Principles, Design, Artifacts, and Recent Advances* (SPIE, Bellingham, WA, 2003), Chap. 10, pp. 37–98.

[11]H. H. Barrett and K. J. Myers, "Series expansions and integral transforms," in *Foundations of Image Science*, edited by B. E. A. Saleh (Wiley, New York, NY, 2004), Chap. 4, pp. 175–214.

[12]H. H. Barrett and K. J. Myers, "Fourier analysis," in *Foundations of Image Science*, edited by B. E. A. Saleh (Wiley, New York, NY, 2004), Chap. 3, pp. 95–174.

[13]H. H. Barrett and K. J. Myers, "Dirac delta and other generalized functions," in *Foundations of Image Science*, edited by B. E. A. Saleh (Wiley, New York, NY, 2004), Chap. 2, pp. 63–94.

[14]S. M. Lea, "Generalized functions in physics," *Mathematics for Physicists* (Brooks-Cole, Belmont, CA, 2004), Chap. 6, pp. 287–322.

[15]T. Mertelmeier, J. Orman, W. Haerer, and M. K. Dudam, "Optimizing filtered backprojection reconstruction for a breast tomosynthesis prototype device," Proc. SPIE **6142**, 61420F-1–61420F-12 (2006).

[16]J. Stewart, "Techniques of integration," in *Calculus: Early Transcendentals*, edited by B. Pirtle and S. Green, 5th ed. (Brooks-Cole, Belmont, CA, 2003), Chap. 7, pp. 474–545.

[17]J. C. Dainty and R. Shaw, "Fourier transforms, and the analysis of image resolution and noise," *Image Science* (Academic, London, England, 1974), Chap. 6, pp. 190–231.

[18]B. Zhao, J. Zhou, Y.-H. Hu, T. Mertelmeier, J. Ludwig, and W. Zhao, "Experimental validation of a three-dimensional linear system model for breast tomosynthesis," Med. Phys. **36**(1), 240–251 (2009).

[19]T. Jing *et al.*, "Amorphous silicon pixel layers with cesium iodide converters for medical radiography," IEEE Trans. Nucl. Sci. **41**(4), 903–909 (1994).

[20]A. R. Cowen, S. M. Kengyelics, and A. G. Davies, "Solid-state, flat-panel, digital radiography detectors and their physical imaging characteristics," Clin. Radiol. **63**, 487–498 (2008).

[21]V. V. Nagarkar, T. K. Gupta, S. R. Miller, Y. Klugerman, M. R. Squillante, and G. Entine, "Structured CsI(Tl) scintillators for x-ray imaging applications," IEEE Trans. Nucl. Sci. **45**(3), 492–496 (1998).

[22]M. Albert and A. D. A. Maidment, "Linear response theory for detectors consisting of discrete arrays," Med. Phys. **27**(10), 2417–2434 (2000).

[23]R. J. Acciavatti and A. D. A. Maidment, "An analytical model of NPS and DQE comparing photon counting and energy integrating detectors," Proc. SPIE **7622**, 76220I-1–76220I-12 (2010).

[24]R. J. Acciavatti and A. D. A. Maidment, "A comparative analysis of OTF, NPS, and DQE in energy integrating and photon counting digital x-ray detectors," Med. Phys. **37**(12), 6480–6495 (2010).